UNIVERSIDADE
BEIRA INTERIOR

ANALYSIS OF THE INFLUENCE OF THE TIP CLEARANCE ON THE PERFORMANCE OF TRANSONIC COMPRESSORS

(versão final após defesa)

Diogo Marques Lopes

Dissertação para obtenção do Grau de Mestre em

Engenharia Aeronáutica

(Mestrado Integrado)

Orientador: Prof. Doutor Francisco Miguel Ribeiro Proença Brójo

fevereiro de 2025

Declaração de Integridade

Eu, Diogo Marques Lopes, que abaixo assino, estudante com o número de inscrição 44463 do Mestrado Integrado em Engenharia Aeronáutica da Faculdade de Engenharia, declaro ter desenvolvido o presente trabalho e elaborado o presente texto em total consonância com o **Código de Integridades da Universidade da Beira Interior**.

Mais concretamente afirmo não ter incorrido em qualquer das variedades de Fraude Académica, e que aqui declaro conhecer, que em particular atendi à exigida referenciação de frases, extratos, imagens e outras formas de trabalho intelectual, e assumindo assim na íntegra as responsabilidades da autoria.

Universidade da Beira Interior, Covilhã 17/02/2025

Diogo Marques Lopes

Acknowledgments

First of all, I would like to thank my supervisor, Professor Francisco Miguel Ribeiro Proença Brójo, for his guidance, support, availability, and all the knowledge he has shared over the months. Thank you for pointing me in the right direction whenever needed.

To my parents, Nelson and Arlete, I owe you my deepest gratitude for the tremendous support, love, and sacrifices you have made for me. I am forever grateful for everything you have done to help me reach this important milestone in my life.

To my girlfriend, Maria, thank you for your constant love, patience, and encouragement. Your support during the most difficult moments of this journey has meant more to me than words can express. I am incredibly grateful to have you by my side.

To my family, for always being there in the most important moments of this journey and for believing in me, thank you so much.

I would also like to thank the incredible friends I have made along the way. Your support, humor, and companionship have been very important during these years. Thank you for sharing this journey with me and for all the unforgettable moments.

Resumo

Na aviação, a eficiência dos compressores é essencial para reduzir custos operacionais e melhorar o desempenho dos motores. Compressores mais eficientes consomem menos combustível, o que diminui as despesas das companhias aéreas. É com esse objetivo em mente que foi realizado este estudo, focando-se na análise de um compressor transónico.

Este estudo explora o desempenho do compressor axial NASA Rotor 67 em duas configurações: com e sem espaçamento na ponta das pás (*tip clearance*). Foram realizadas simulações de dinâmica de fluidos computacional para avaliar os efeitos do espaçamento na ponta nas características do escoamento e na eficiência global do compressor.

O espaçamento na ponta das pás refere-se ao pequeno espaço entre as pontas das pás de um rotor e o invólucro circundante nas turbomáquinas. Esta folga é necessária e intencionalmente concebida para permitir a expansão térmica, as tolerâncias mecânicas e a deformação estrutural durante o funcionamento, de modo a garantir que as pás não entrem em contacto direto com a carcaça.

Neste estudo, o software Ansys CFX foi utilizado para analisar o desempenho aerodinâmico do compressor transónico em condição estacionária, tendo sido utilizado o modelo SST k-ω para as simulações. O Ansys CFX permite simular com precisão os fenómenos de escoamento complexos presentes nas turbomáquinas, incluindo os efeitos da compressibilidade.

A análise focou-se em métricas de desempenho críticas, como a razão de pressão e a eficiência, comparando os dois modelos para compreender o impacto do espaçamento nas características do escoamento. Foram utilizadas isolinhas do número de Mach relativo e das distribuições de pressão para estudar o comportamento do escoamento em diferentes secções do rotor, destacando as principais diferenças entre os dois casos.

Os resultados demonstraram que a ausência de espaçamento melhora o desempenho, alcançando razões de pressão mais elevadas e padrões de escoamento mais uniformes junto às pontas das pás, onde as irregularidades induzidas pelo espaçamento foram mitigadas. Isto era esperado, uma vez que o espaçamento está associado a perdas que reduzem a eficiência global.

Palavras-chave

Rotor 67; Compressor transónico; Espaçamento na ponta da pá; Ansys CFX;

Abstract

In aviation, compressor efficiency is essential for reducing operating costs and improving engine performance. More efficient compressors consume less fuel, which reduces airlines' expenses. It is with this goal in mind that this study was carried out, focusing on the analysis of a transonic compressor.

This study explores the performance of the NASA Rotor 67 axial compressor in two configurations: with and without tip clearance. Computational fluid dynamics simulations were carried out to evaluate the effects of tip clearance on the flow characteristics and overall efficiency of the compressor.

Tip clearance refers to the small gap between the blade tips of a rotor and the surrounding casing in turbomachinery. This gap is necessary and intentionally designed to allow for thermal expansion, mechanical tolerances, and structural deformation during operation to ensure that the blades do not come into direct contact with the casing.

In this study, Ansys CFX software was used as a tool to analyze the aerodynamic performance of the transonic compressor under steady-state conditions, and the model used for the simulations was the SST k-ω turbulence model. Ansys CFX makes it possible to accurately simulate the complex flow phenomena present in turbomachinery, including the effects of compressibility.

The analysis focused on critical performance metrics such as pressure ratio and efficiency, comparing the two models to understand the impact of the gap on flow characteristics. Contours of the relative Mach number and pressure distributions were used to study the flow behavior in different sections of the rotor, highlighting the main differences between the two cases.

The results showed that the absence of spacing improves performance, achieving higher pressure ratios and more uniform flow patterns near the blade tips, where the irregularities induced by spacing were mitigated. This was expected, as tip clearance is associated with leaked losses, which can reduce overall efficiency.

Keywords

Rotor 67; Transonic compressor; Tip Clearance; Ansys CFX;

CONTENTS

Figure List

Table List

List of Acronyms

2D	Two dimensional
3D	Three dimensional
CAD	Computer aided design
CCEA	Cooperative coevolution algorithm
CCG	Circumferential casing grooves
CFD	Computational fluid dynamics
GRC	Glenn Research Center
GSF	Global size factor
IGV	Inlet guide vanes
NASA	National Aeronautics and Space Administration
RI	Rotating Instability
RMS	Root mean square
SST	Shear-stress transport
TLV	Tip Leakage Vortex

Nomenclature

F_1	Blending function	
G	Production term of turbulent kinetic energy	$[\mathrm{kg/m.s^3}]$
k	Turbulent kinetic energy	$[\mathrm{m^2/s^2}]$
M	Mach number	
P	Pressure	[Pa]
P_t	Total (stagnation) pressure	[Pa]
PR	Pressure ratio	
S	Entropy	$[\mathrm{J/K}]$
T	Temperature	[K]
t	Time	[s]

Greek Letters

β	Empirical coefficient	
β^*	Empirical coefficient	
γ	Empirical coefficient	
κ	Ratio of specific heats	
μ	Dynamic viscosity	$[\mathrm{kg/m.s}]$
μ_t	Turbulent viscosity	$[\mathrm{kg/m.s}]$
ν_t	Turbulent kinematic viscosity	$[\mathrm{m^2/s}]$
ρ	Density	$[\mathrm{kg/m^3}]$
σ_k	Empirical coefficient	
σ_ω	Empirical coefficient	
$\sigma_{\omega 2}$	Empirical coefficient	
ω	Specific dissipation rate	$[\mathrm{1/s}]$

CHAPTER 1 – MOTIVATION AND OBJECTIVES

1.1 Motivation

Gas turbines had their first practical applications in the early 20th century, primarily developed for use in industrial and power generation applications. Later, during World War II, there was a significant push in their development for use in military aircraft. After the war, there was a rapid expansion in the aerospace industry, driven largely by the continuous development of more advanced jet engines.

In recent decades, there have been significant advancements in gas turbine technology, including improvements in efficiency, emissions reduction, increased lifespan, and greater operational flexibility. This has been driven by advances in areas such as materials, aerodynamics, combustion control, and cooling technologies, among others.

Transonic compressors represent a significant technological advancement, playing a pivotal role in the advancement and efficacy of modern jet engines. They enable operation over a broader range of speeds and altitudes, improving fuel efficiency. These compressors also enable greater power and performance, making them essential for the ongoing advancement of aviation and related technologies.

The influence of tip clearance is a critical factor in turbomachinery performance, directly affecting efficiency, pressure loss, and flow structures near the blade tip. Understanding its effects is essential for optimizing aerodynamic design, minimizing energy dissipation, and improving overall rotor performance, especially in transonic conditions.

NASA Rotor 67 is a widely studied transonic axial compressor rotor, making it an ideal choice for this analysis. Its well-documented geometry and extensive experimental and numerical data provide a reliable benchmark for validation.

1.2 Objectives

The main objective of this study is to numerically estimate the influence of the tip clearance effects on the performance of transonic compressors (Rotor 67). This study therefore has the following specific objectives:

- To understand the operation of compressors and how the tip clearance influences their performance;
- To carry out a comparative study of different simulations.

CHAPTER 2 – LITERATURE REVIEW

2.1 Gas Turbines

In essence, the gas turbine engine is a heat engine that generates thrust by using air as its working fluid. This can only be accomplished by increasing the kinetic energy of the air as it passes through the engine. This increase is achieved by first increasing the pressure energy, then adding heat energy, and finally converting back to kinetic energy in the form of a high velocity jet efflux [1].

To achieve expansion within a turbine, a pressure ratio needs to be established, making compression of the working fluid the initial and crucial step in the gas turbine plant cycle. Boosting the power generated by the turbine can be accomplished by adding energy to elevate the temperature of the working fluid before expansion. When the working fluid is air, an effective method to achieve this is by combusting fuel within the compressed air. The expansion of the heated working fluid results in increased power output from the turbine, enabling it to deliver a useful output beyond driving the compressor. This configuration embodies the gas turbine or internal-combustion turbine in its most basic iteration. The three primary components: compressor, combustion chamber, and turbine are interconnected as illustrated diagrammatically in Figure 1 [2].

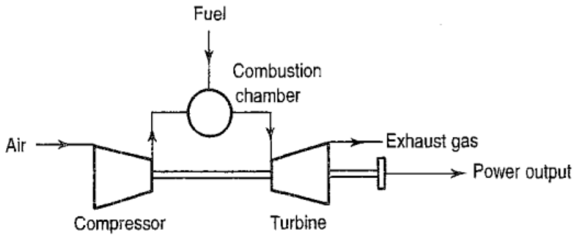

Figure 1. Simple gas turbine system [2]

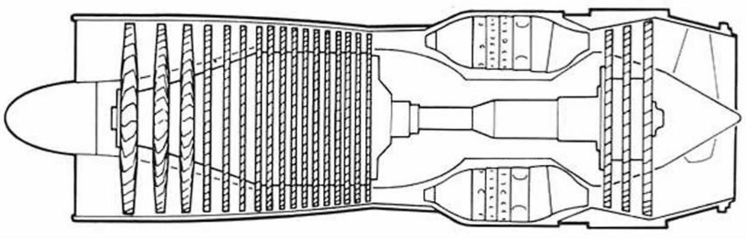

Figure 2. Turbojet engine [1]

The gas turbine engine operates in a manner comparable to the four-stroke piston engine. However, combustion takes place under constant pressure in the gas turbine engine, while in the piston engine it occurs under constant volume. Induction, compression, combustion, and exhaust occur in both engine cycles. In the piston engine, these processes are intermittent, while in the gas turbine, they are continuous as shown in Figure 2 [1].

2.1.1 Ideal Brayton Cycle

Figure 3 illustrates a T-s diagram depicting the Brayton cycle. Originating from free stream conditions at station 0, during cruise, the inlet decelerates the airflow as it reaches the compressor face at station 2. As the airflow slows down, a portion of the kinetic energy associated with the aircraft velocity elevates the static pressure of the air, compressing the flow. In an ideal scenario, this compression would be isentropic, simultaneously increasing the static temperature as depicted in Figure 3. The compressor does work on the gas, isentropically raising both pressure and temperature to station 3, the compressor exit. While the compression is ideally isentropic, the real T-s diagram would illustrate a deviation due to the actual increase in entropy during the compression process, leaning the compression process line towards the right. The combustion process in the burner occurs at constant pressure from station 3 to station 4. The fuel-air ratio and the type of fuel influence the increase in temperature. The heated exhaust then passes through the power turbine, where work is done by the flow from station 4 to station 5. Given that the turbine and compressor are situated on the same shaft, the work done on the turbine matches that of the compressor, ideally resulting in the same temperature alteration. Finally, the nozzle returns the flow isentropically to free stream pressure from station 5 to station 8, restoring external flow conditions to free stream status and thereby completing the cycle [3].

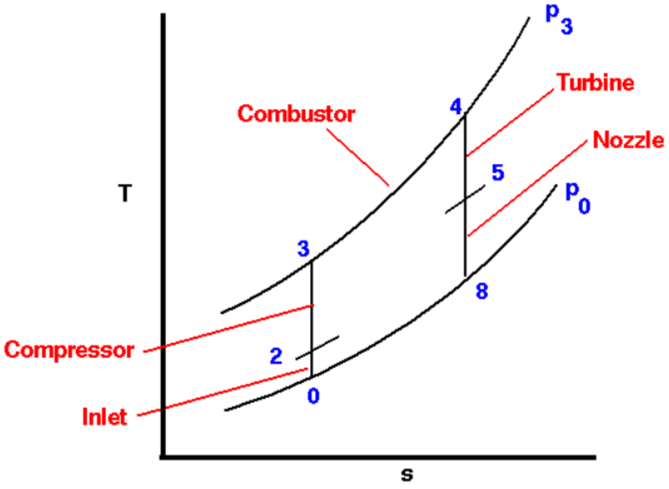

Figure 3. Ideal Brayton cycle T-s diagram [3]

2.1.2 Types of compressors

Figure 4a and Figure 4b depict two types of compressors: the one on the right is known as an axial compressor, characterized by the flow moving parallel to the rotation axis, while the compressor on the left is termed a centrifugal compressor, where the flow is directed perpendicular to the axis of rotation [4].

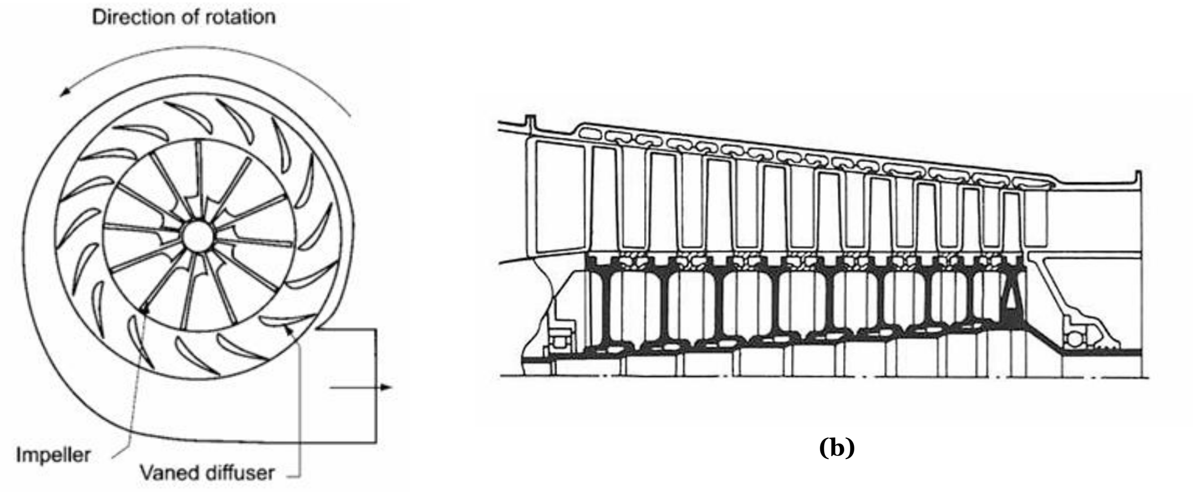

(b)

(a)

Figure 4. Centrifugal compressor (a) [5]; **Axial compressor (b)** [1]

On average, a single-stage centrifugal compressor can boost pressure by a factor of 4, while a similar single-stage axial compressor only increases it by a factor of 1.2. However, it is comparatively straightforward to connect multiple stages and create a multistage axial compressor. In this setup, pressure is multiplied from stage to stage (8 stages at 1.2 per stage result in a factor of 4.3). Creating an efficient multistage centrifugal compressor is much more challenging because the flow needs to be redirected to the axis at each stage. Due to the flow being turned perpendicular to the axis, engines with centrifugal compressors tend to be wider, with a greater cross-sectional area than their axial counterparts, leading to increased aircraft drag, an undesirable consequence. Hence, most high-performance turbine engines that require high compression employ multistage axial compressors. However, if only a moderate level of compression is needed, a centrifugal compressor offers a simpler solution [4].

Centrifugal

A centrifugal compressor comprises several components: inlet guide vanes, an inducer, an impeller, a diffuser, and a scroll as shown in Figure 5. Inlet Guide Vanes (IGVs) are exclusively employed in high-pressure ratio transonic compressors. The fluid enters the compressor through an intake duct, where the IGVs provide prewhirl to it. Subsequently, the fluid passes into an inducer without any incidence angle, transitioning its flow direction from axial to radial. As it traverses the impeller, the fluid is given energy from the rotor while undergoing compression. It is then directed into a diffuser, where kinetic energy is converted into static pressure. Finally, the flow enters the scroll, from which the discharge is taken [6].

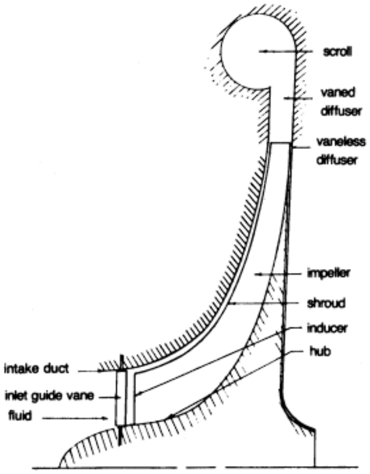

Figure 5. Schematic of a centrifugal compressor [6]

Axial

The axial-flow compressor compresses its working fluid by initially speeding up the fluid and then diffusing it to achieve a pressure rise. This acceleration occurs through a series of rotating blades known as the rotor, while the diffusion is facilitated by a set of stationary blades called the stator. The stator's role is to convert the velocity increase from the rotor into a pressure increase. Compressors typically consist of multiple stages, with each stage comprising one rotor and one stator. To ensure that air enters the first-stage rotor at the desired angle, an additional row of blades, known as Inlet Guide Vanes (IGVs), is often employed at the compressor inlet. Apart from the stators, another diffuser positioned at the compressor exit further diffuses and regulates the velocity of the airflow entering the combustors [6].

In an axial compressor, air proceeds from one stage to another, with each stage incrementally elevating the pressure. By generating modest pressure increments (ranging from 1.1:1 to 1.4:1), exceptionally high efficiencies can be achieved. This minimal pressure elevation also simplifies the computational calculations involved in compressor design [6].

Figure 6 illustrates the variation in pressure and velocity throughout the passage of flow across multiple stages of an axial compressor. As depicted in Figure 6, the length of the blades and the annulus area, defined as the area between the shaft and the shroud, diminishes along the length of the compressor. This reduction in flow area counterbalances the rise in fluid density during compression, thereby maintaining a consistent axial velocity. In the initial compressor design, the average blade height is typically employed as the blade height for each stage [6].

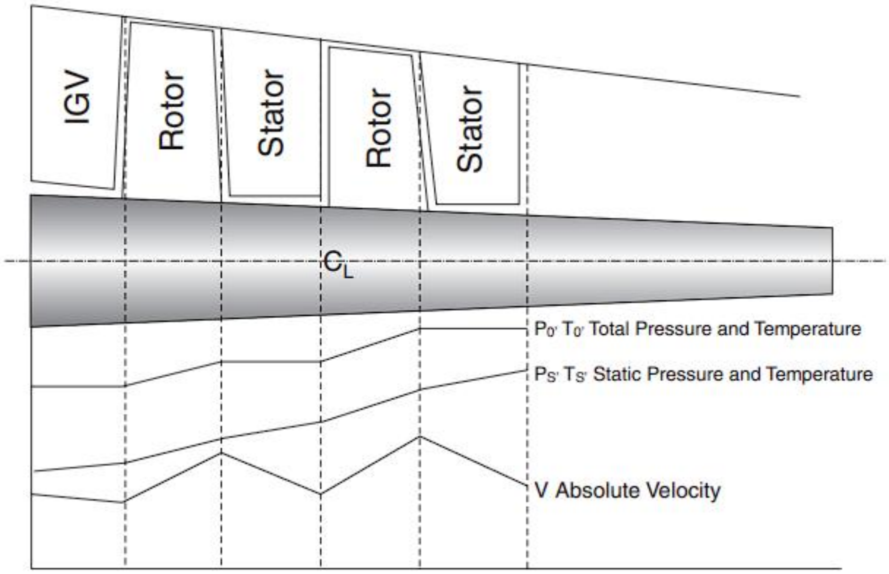

Figure 6. Variation of velocity and pressure through an axial-flow compressor [6]

Compressor stall and compressor surge

The operation of a jet engine is limited by the onset of compressor stall. Both rotational stall and surge are incompletely understood, particularly with respect to the mechanisms that initiate and propagate these instabilities, as well as the aerodynamic loads imposed on individual turbomachinery components during such events. As a result, a conservative approach is often taken to blade and casing design, which limits the nominal operating envelope of the engine [7].

Aerodynamic instability, manifested as stall and surge, occurs when a compressor operates at reduced mass flow. Surge is characterized by oscillation of the annulus-averaged flow throughout the system, potentially leading to flow reversal, also known as backflow. Based on the amplitude of the system oscillations and the presence of backflow, surge is classified as either mild or deep. Mild surge involves minor flow oscillations, accompanied by a slight reduction in efficiency and increased noise levels. In contrast, deep surge results in severe instability, causing large oscillations in pressure and mass flow, often accompanied by a violent hammering sound and potentially catastrophic failure [8].

Stall always precedes surge, although it does not necessarily cause it. Most studies suggest that localized micro-instabilities, known as stall cells, develop and propagate circumferentially. Two primary stall initiation mechanisms have been widely recognized: modal type and spike type, distinguished by differences in circumferential propagation speed and fluctuation amplitude. The modal type is associated with small amplitude disturbances that propagate circumferentially at 20-50% of impeller speed. In some cases, modal type is followed by spike type, which is a sudden onset of turbulence. This is typically observed as an upward spike in the transient pressure curve and a downward spike in the velocity curve, with a higher circumferential propagation speed than the modal type [8].

Transonic compressors

When we refer to a transonic compressor, we are describing an axial flow compressor where the inlet flow Mach number, in relation to the rotating blades, changes from being below one at the inner casing or hub to significantly above one at the blade's tip. Typically, the flow is diffused to subsonic velocities within the flow passages created by the rotating blades, contributing to a portion of the desired pressure increase [9].

Research and development initiatives have focused on axial flow compressors for around 80 years, while transonic compressors have been a subject of investigation for nearly 70 years. The initial systematic inquiries in the United States were spearheaded by the Lewis Research Center of the NASA around 1950, and the technology was promptly harnessed for incorporation into the initial turbofan engine iterations. Given its capacity to deliver elevated pressure ratios per stage and greater airflows per unit of engine frontal area compared to subsonic compressors, the transonic compressor has evolved into a pivotal element of all contemporary aircraft engines [9].

2.2 Rotor 67

NASA rotor 67 (Figure 7) is a transonic axial flow compressor with 22 blades, originally designed and tested at NASA's Lewis Research Center in the late 70s. The blade geometry and experimental aerodynamic data obtained at NASA were subsequently utilized to establish a blind test case in the 90s, aimed at validating numerical methods.

Table 1. Aerodynamic design parameters [10]

Number of blades	22
Inlet hub/tip ratio	0.375
Exit hub/tip ratio	0.478
Design rotational speed	16043 rev/min
Tip solidity	1.29
Tip clearance	1.01 mm
Tip speed	429 m/s
Design pressure ratio	1.63
Design mass flow rate	33.25 kg/s

Regarded as a classic test case representing intricate three-dimensional viscous flow in transonic blade configurations, rotor 67 is also employed as a case study for aerodynamic optimization techniques. In this context, rotor 67 stands as a standardized benchmark. Detailed information regarding the geometry and operational conditions can be found in the original reports, which are summarized in the Table 1.

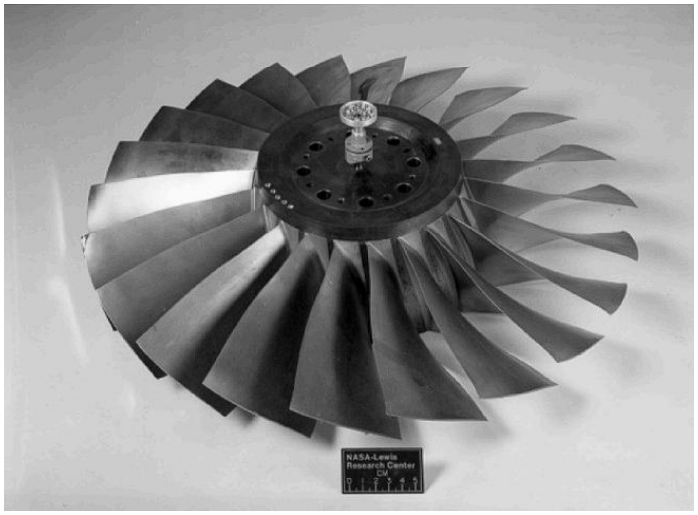

Figure 7. NASA rotor 67 [10]

2.3 Key Parameters and Recent Studies on Transonic Rotors

The performance of transonic compressors is strongly influenced by geometrical factors that affect aerodynamic efficiency and shock wave behavior. Blade geometry is critical, with parameters such as aspect ratio, camber, stagger angle and leading and trailing edge designs playing a central role in determining flow deflection, pressure rise, shock formation and boundary layer behavior. Tip clearance also has a significant effect on leakage and overall losses.

Flow path characteristics such as hub-to-tip ratio, meridional contour and interstage gaps further influence radial flow distribution, pressure gradients and wake recovery. Shock control is achieved through features such as leading-edge sweep, blade bow and lean, which help to spread the shock load and reduce pressure gradients, with some designs even incorporating trailing edge blowing or slotting.

In addition, tip and endwall treatments such as casing grooves and endwall contouring are used to manage leakage and secondary flow structures. Optimization of these geometric parameters is essential to balance performance, efficiency and stability in transonic compressors.

2.3.1 Blade profile

Blade profile studies are essential in transonic rotors to optimize performance, efficiency, and durability. In these rotors, shock waves are created due to the velocities at the blade tips. By studying and refining the blade profile, shock formation can be managed or delayed, which reduces energy losses associated with shock, minimizes drag, and helps prevent flow separation.

A study conducted by P. Song and J. Sun in 2015 [11], aimed to reduce shock waves and minimize losses in blade design by simultaneously adjusting both blade section profiles and stacking lines, allowing greater flexibility in blade shape optimization. A global optimization method is incorporated into the blade shape design (Figure 8), including an improved CCEA (Cooperative Coevolution Algorithm) optimizer. The method is used to optimize the transonic NASA Rotor 67 in design flow, showing pressure ratio and efficiency improvements of 6.53% and 1.27%, respectively.

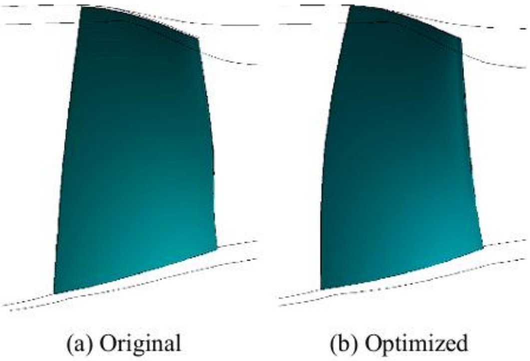

Figure 8. Meridional view for original and optimized blade geometry [11]

In order to minimize fuel consumption and engine weight, an effective way to improve the aerodynamic performance of transonic compressor stages is to sweep and lean the rotor blades (Figure 9). In fact, as shown in the 2019 study by N. Z. Huang et al. [12], using Rotor 37, the leaned rotor had a 1.1% improvement in efficiency and the total pressure ratio remained largely unchanged. The swept rotor had a 0.2% improvement in efficiency and a 0.8% improvement in pressure ratio. At peak efficiency, the swept and leaned rotor performed better than the others, with a predicted efficiency of 1.1% and a total pressure ratio of 1.6% higher than rotor 37.

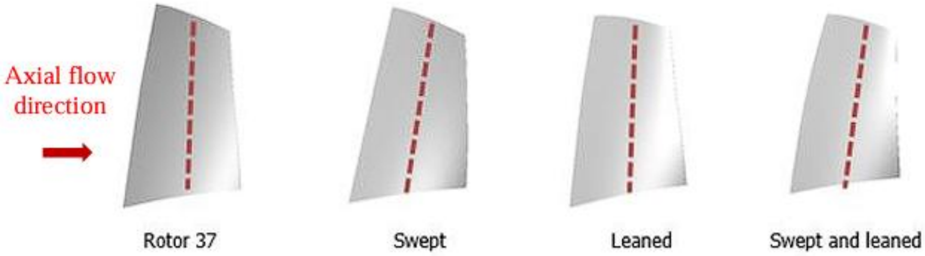

Figure 9. Meridional view for the different blade alignments [12]

2.3.2 Slot Casing Treatments

In order to increase the operational stability of a transonic axial compressor, a study in 2013 by J. H. Kim et al. [13], with optimized circumferential casing grooves was carried out. One of the main causes of induced surge and stall in an axial compressor is known to be the tip leaking vortex. The stability of an axial compressor is significantly impacted by the trajectory of the tip leakage vortex, which is influenced by the geometry close to the tip area. Circumferential casing grooves (CCGs) have been used as a casing treatment technique to regulate this flow phenomena as shown in Figure 10.

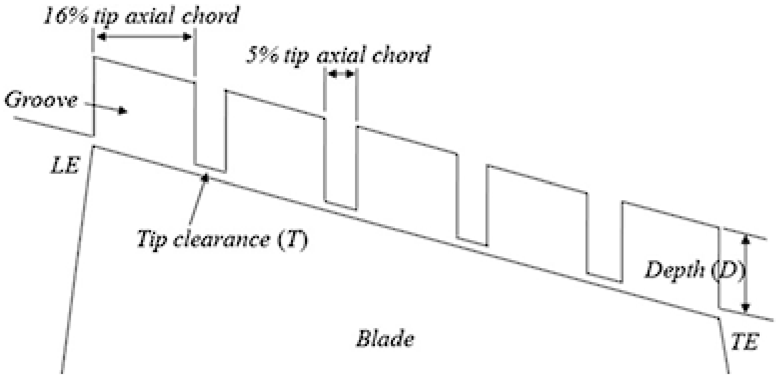

Figure 10. Tip clearance and the circumferential casing grooves [13]

According to the shape optimization findings, the peak adiabatic efficiency dropped by only 0.18% with almost the same total pressure ratio as the smooth casing, but the stall margin for the optimal design with the CCGs increased by 5.13% [13].

2.3.3 Air Injection

The efficiency, stability, and operating range may be improved by investigating the impacts of air injection as it can advantageously alter flow patterns, postponing the onset of stall and lowering losses related to shock-boundary layer interactions. Additionally, this method can enhance pressure recovery, increasing the compressor's dependability and efficiency under a variety of operating circumstances.

A 2021 study by C.-T. Dinh and K.-Y. Kim [14] conducted a parametric analysis of the effects of stator air injection on a single-stage transonic axial compressor's aerodynamic performance demonstrated that the adiabatic efficiency and total pressure ratio are significantly impacted by the injection mass flow rate. The maximum values of the total pressure ratio and peak adiabatic efficiency were 2.0090 and 85.64%, respectively, at 2.0% mass flow rate of injection. When compared to smooth casing, these data show that the compressor performs significantly better as the peak adiabatic efficiency, and total pressure ratio are 83.85% and 2.0045. Unfortunately, stator injection did not significantly increase the stall margin as the highest stall margin was 10.66%, whereas for smooth casing, the stall margin was 9.95%.

2.3.4 Tandem rotor bladings

In order to study the performance of tandem rotor blades M. Mohsen and M. M. E. Eg in 2017 [15] proposed a tandem rotor design (Figure 11) with same inflow characteristics of the reference transonic rotor ‘NASA Rotor 37’ was conducted. The computational findings demonstrate significant enhancements in flow turning and diffusion without encountering flow separation. In comparison to the baseline rotor 'NASA Rotor 37', the tandem design exhibits a 17% increase in total pressure ratio and a 2% increase in rotor adiabatic efficiency.

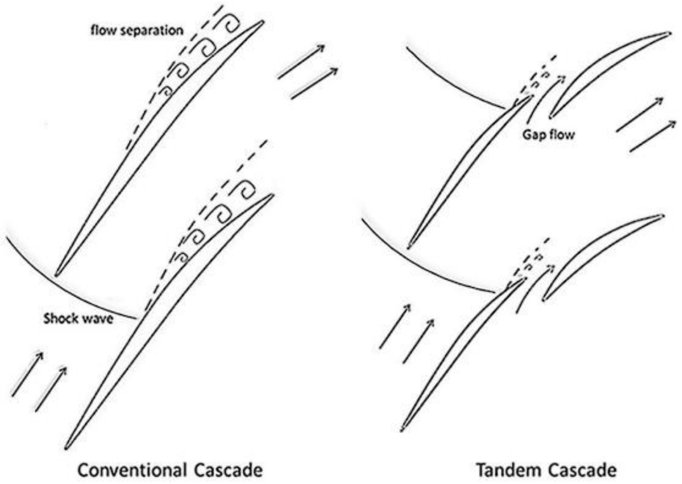

Figure 11. Layout of conventional and tandem cascades [15]

2.4 Tip Clearance

Tip clearance refers to the small gap between the blade tips of a rotor and the surrounding casing in turbomachinery as illustrated in Figure 12. This gap is intentionally designed to account for thermal expansion, mechanical tolerances, and structural deformation during operation to ensure that the blades do not come into direct contact with the casing.

However, the presence of tip clearance introduces aerodynamic challenges, such as leakage flow through the gap, which disrupts the main flow path and reduces the efficiency of the rotor. This leakage flow can also lead to complex phenomena such as tip vortices, increased turbulence and local flow separation, all of which contribute to aerodynamic losses and can affect the overall performance and stability of the compressor.

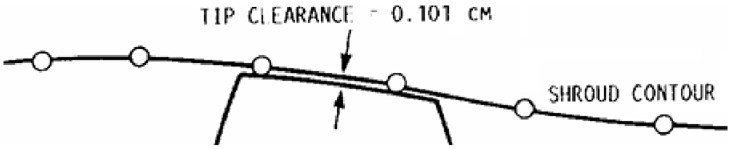

Figure 12. NASA Rotor 67 tip clearance close-up [10]

2.4.1 Recent Studies on Tip Clearance Effects

Recent studies of tip leakage effects have focused on their impact on aerodynamic performance, efficiency, and losses in turbomachinery. Researchers have investigated how tip leakage flow interacts with the main flow, resulting in secondary flow structures and reduced overall efficiency.

Advances in computational fluid dynamics (CFD) and experimental techniques have provided deeper insights into flow physics, including unsteady effects and blade tip modifications to mitigate losses. In addition, studies have investigated the role of tip clearance in transonic and supersonic conditions, where shock-tip leakage interactions become critical.

A study in 2016 by S. N. Danish et al. [16] showed that both stage efficiency and pressure ratio improve as the tip gap decreases. A smaller gap offers better performance, but practical limitations make very low gaps difficult to achieve. Larger clearances result in significant reductions in efficiency and pressure ratio. While a moderate gap provides a good balance, a slightly larger one allows for a wider operating range, but with some compromise in performance.

S. S. Kumar et al. in 2018 [17] conducted an analysis of how non-uniform rotor tip clearances affect the performance of a transonic axial flow compressor. The investigation revealed that asymmetric tip clearances in the compressor have a negligible effect on the overall performance of the compressor stage. Despite the variation, the performance parameters such as efficiency and pressure ratio remain largely unaffected. This suggests that in this case, asymmetric tip clearance does not contribute significantly to aerodynamic losses or efficiency reduction.

A 2020 study by T. Liang et al. [18] identified an optimal tip gap combination for a counter-rotating axial compressor: half the design gap for Rotor 1 and a quarter of the design gap for Rotor 2. This configuration improved peak efficiency by 0.63% and stability margin by 29.4%. Increasing the tip clearance shifts the initial position of the Tip Leakage Vortex (TLV) downstream, increases its scale and intensity, and causes its trajectory to deflect circumferentially toward the inlet. The tip flow of one rotor is affected by the clearance variation of the other, with this effect being more pronounced near stall conditions than at peak efficiency. The first rotating stall stage is also affected by the tip clearance of both rotors, with a larger clearance in Rotor 1 or a smaller clearance in Rotor 2 causing the first stall stage to shift from Rotor 2 to Rotor 1.

In 2021, B. Zhang et al. [19] conducted a study that indicated that stall mechanisms vary with tip clearance size. For larger clearances, stall is predominantly triggered by intensified tip leakage flow, whereas smaller clearances lead to stall due to the combined effects of tip leakage flow and boundary layer separation. This distinction highlights the intricate interaction between leakage flow dynamics and boundary layer behavior in determining compressor stability.

In the 2021 study by T. Li, Y. Wu, and H. Ouyang [20], full-annulus numerical simulations were performed to investigate how different tip clearance sizes affect Rotating Instability (RI) in a low-speed axial compressor. The study found that increasing the tip clearance size increases the TLV, resulting in greater flow unsteadiness and a higher probability of RI occurrence. In addition, the research showed that larger tip clearances result in more pronounced pressure fluctuations near the rotor tip, which can adversely affect the aerodynamic performance and stability of the compressor. These findings underscore the importance of optimizing tip clearance dimensions to mitigate RI and improve compressor efficiency.

2.5 Mass and Momentum Conservation

Computational Fluid Dynamics relies on mathematical models to simulate fluid behavior, and the foundation of these models is the set of governing equations that describe fluid motion. Among them, the continuity equation ensures conservation of mass, while the momentum equations determine how forces affect velocity. Together, these equations form the Navier-Stokes equations, which are fundamental to predicting flow patterns, pressure distributions, and aerodynamic performance in any CFD analysis.

The continuity equation ensures that mass is conserved in a fluid flow. It states that the rate of mass entering a control volume must be equal to the rate of mass leaving, taking into account density variations in compressible flows. In CFD simulations, this equation is essential for accurately predicting velocity fields and maintaining physically realistic flow behavior.

$$\frac{\delta \rho}{\delta t} + \mathit{\Delta} \cdot (\rho u) = 0 \ (1)$$

The momentum equations describe how fluid velocity changes due to pressure, viscous forces, and external influences. They are derived from Newton's second law and solved in three directions: x, y, and z. These equations, along with the continuity equation, form the Navier-Stokes equations that govern all fluid motion. They are critical for capturing flow acceleration, turbulence effects, and interactions with solid boundaries, making them fundamental to all CFD applications.

$$\rho\left(\frac{\delta u}{\delta t}+u\frac{\delta u}{\delta x}+v\frac{\delta u}{\delta y}+w\frac{\delta u}{\delta z}\right)=-\frac{\delta \rho}{\delta x}+\mu\nabla^{2}u+F_x \ (2)$$

$$\rho\left(\frac{\delta v}{\delta t}+u\frac{\delta v}{\delta x}+v\frac{\delta v}{\delta y}+w\frac{\delta v}{\delta z}\right)=-\frac{\delta \rho}{\delta y}+\mu\nabla^{2}v+F_y \ (3)$$

$$\rho\left(\frac{\delta w}{\delta t}+u\frac{\delta w}{\delta x}+v\frac{\delta w}{\delta y}+w\frac{\delta w}{\delta z}\right)=-\frac{\delta \rho}{\delta z}+\mu\nabla^{2}w+F_z \ (4)$$

CHAPTER 3 – METHODOLOGY AND MODELLING

This chapter describes the general process for conducting a CFD analysis as well as the different methods and steps applied in this study, serving as a reference for comprehending the different elements involved in the CFD simulation and analysis.

Several factors can affect the quality of a CFD simulation and should be carefully considered. Gaps, small edges or sharp angles can distort the mesh in CFD simulations, leading to poor convergence and numerical instability. Mesh quality plays a critical role, as finer meshes capture more detail but require more computational resources, and poor mesh quality can lead to inaccuracies or convergence problems. Boundary conditions are essential to define physical constraints; if they aren't set correctly, the results can deviate significantly from reality. The choice of turbulence model is also critical; it should match the flow characteristics, as an inappropriate model can cause discrepancies in the prediction of turbulent effects. Solver settings, such as convergence criteria and numerical schemes, affect both accuracy and stability.

The simulations in this study were conducted using Ansys Workbench, specifically the Geometry, TurboGrid, and CFX modules as shown in Figure 13. The steps of said modules are:

1. Geometry (Geometry module)
2. Turbo Mesh (TurboGrid module)
3. Setup (CFX module)
4. Solution (CFX module)
5. Results (CFX module)

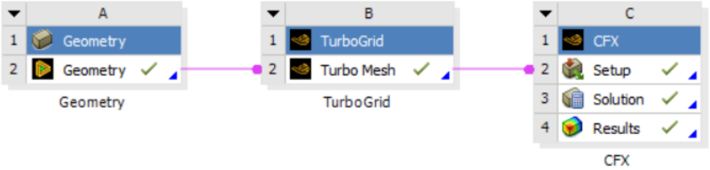

Figure 13. Structure of modules in Ansys Workbench for rotor analysis

ANSYS CFX was chosen for these simulations due to its robust capabilities in handling the complex rotational flows inherent to turbomachinery. Its predefined modes for periodicity, rotating domains, and passage flow allow for an efficient and accurate representation of the rotor's aerodynamics.

Additionally, CFX employs the finite volume method, ensuring accurate conservation of mass, momentum, and energy across control volumes. Its seamless integration with TurboGrid, which was used for mesh generation, ensures a streamlined workflow and optimized mesh quality tailored for turbomachinery applications. These features make CFX particularly well-suited to this study.

3.1 Geometry

This step involves creating or importing the physical model (geometry) that represents the domain of interest in which fluid flow is to be simulated.

The geometry is a 2D or 3D representation of the object or system, such as an aircraft wing, pipe, or room, where the fluid (liquid or gas) interacts with solid boundaries. It can be constructed using CAD software or imported from external design files. It's critical to ensure that the geometry accurately captures the physical features and boundaries required for the simulation, although geometric approximations and simplifications may be necessary to enable analysis at an acceptable level of effort.

In this study, two different models were tested, one of which has a tip clearance. This is the only difference between both models. However, this is only reflected in the mesh step, so the geometry without the tip clearance is used.

The Rotor 67 geometry (Figure 14) was imported into DesignModeler and edited. A sketch was created to design and name the various sections important to the flow path, such as the inlet, outlet, shroud, and hub. The FlowPath tool was then used to generate and define the flow passage.

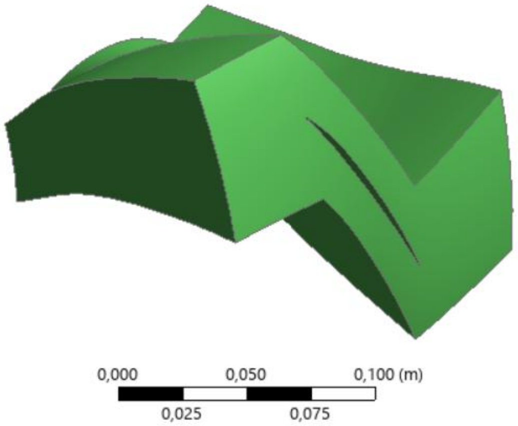

Figure 14. Geometry isometric view

3.2 Mesh

In this step the geometry is divided into small, discrete elements known as cells or elements, which will be used for solving the governing fluid flow equations.

The quality of the mesh, including element size, density, and distribution, directly affects the accuracy and computational efficiency of the simulation. Areas of interest, such as boundary layers or regions with high gradients, often require finer meshing. Therefore, it is then necessary to define mesh refinement, ensure mesh quality metrics (orthogonality, skewness will be used in this study), and balance mesh resolution with computational cost.

3.2.1 Mesh Quality

In order to ensure good mesh quality, two different criteria will be examined: mesh orthogonality and skewness.

The degree to which the angles between neighboring element faces or edges resemble an ideal angle (typically 90° for structured meshes) is known as mesh orthogonality. Bad orthogonality in a mesh means the cell faces deviate significantly from 90° angles, causing alignment issues with the flow. This leads to increased numerical diffusion, reduced accuracy in capturing gradients, slower or non-converging solutions, and higher computational cost due to extra corrective terms. To prevent this, the orthogonality angle should always be greater than 20° being calculated as $90 - a\cos{(n \cdot s)}$ [21].

In Figure 15 it is the angle between the vector that joins two mesh (or control volume) nodes (s) and the normal vector for each integration point surface (n) associated with that edge. Significant orthogonality and non-orthogonality are illustrated at $ip1$ and $ip2$, respectively [21].

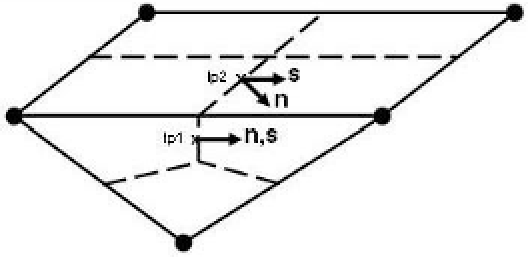

Figure 15. Mesh orthogonality in CFX [21]

Skewness in a mesh measures how much a cell shape deviates from its ideal configuration, like an equilateral triangle or a square (Figure 16). A high skewness value in a mesh means the cell shapes deviate significantly from their ideal geometry.

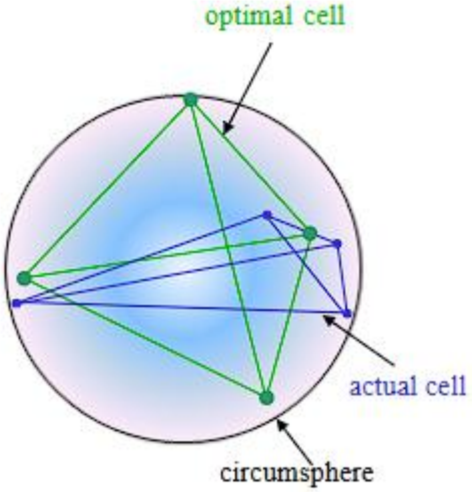

Figure 16. Comparison of an optimal cell and the actual cell [22]

Table 2. Mesh Skewness Quality Values [22]

Value of Skewness	Cell Quality
0 - 0.25	Excellent
0.25 - 0.50	Good
0.50 - 0.75	Fair
0.75 - 0.95	Poor
0.95 - <1	Bad
1	Degenerate

Table 2 lists the range of skewness values and corresponding cell quality.

3.2.2 Mesh Independence

A mesh independence test, also known as a mesh convergence study, is used in CFD to ensure that simulation results do not depend on the mesh resolution. The process involves running simulations with increasingly finer meshes and comparing key results, such as pressure, velocity, or force, across these meshes. The goal is to find the mesh level at which these results stabilize, meaning they no longer change significantly with further refinement. This optimal mesh strikes a balance between accuracy and computational efficiency, ensuring that the solution is reliable and not affected by the mesh quality itself.

In this study, several meshes with different Global Size Factors (GSFs) were used to achieve mesh independence, and the parameter studied was the pressure ratio. The GSFs are a scaling parameter that globally controls the size of mesh elements. A lower GSF results in larger elements, reducing the total number of elements and computational cost at the expense of resolution, while a higher GSF produces smaller elements, increasing mesh density and improving accuracy but requiring more computational resources.

3.2.3 TurboGrid

TurboGrid is an Ansys tool designed for high-quality hexahedral meshing in turbomachinery applications, such as compressors. It automates mesh generation for complex blade geometries, improving both accuracy and efficiency in simulations. With advanced controls for boundary layers and specific geometry features like tip gaps, TurboGrid enables detailed, precise meshes that capture critical flow characteristics.

3.2.3.1 Tip Clearance Model

In this step, the shroud tip feature in TurboGrid was used to define a specific tip clearance of 1.01mm for one of the simulations. The mesh was then generated as shown in Figure 17a and Figure 17b:

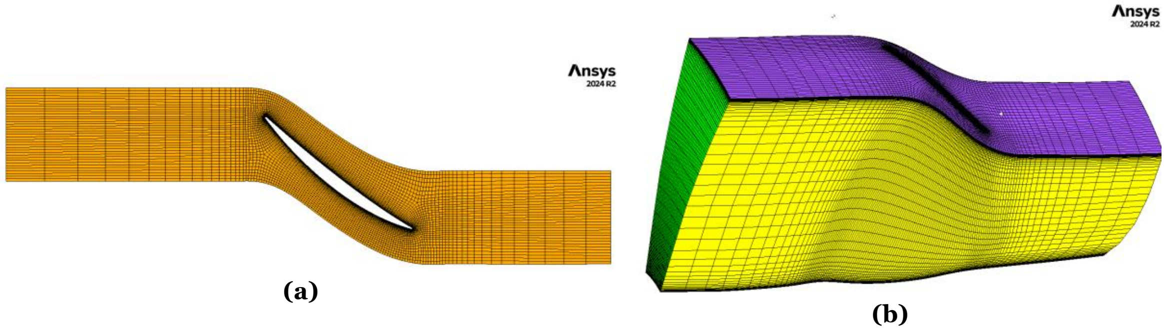

(a) **(b)**

Figure 17. Mesh views: (a) blade-to-blade; (b) 3D view

As mentioned earlier, the five different meshes used for the independence study differ in the GSF. The GSFs used were 0.8, 1.0, 1.2, 1.3 and 1.4. As for the rest of the parameters, the default settings were used as presented in Figure 18.

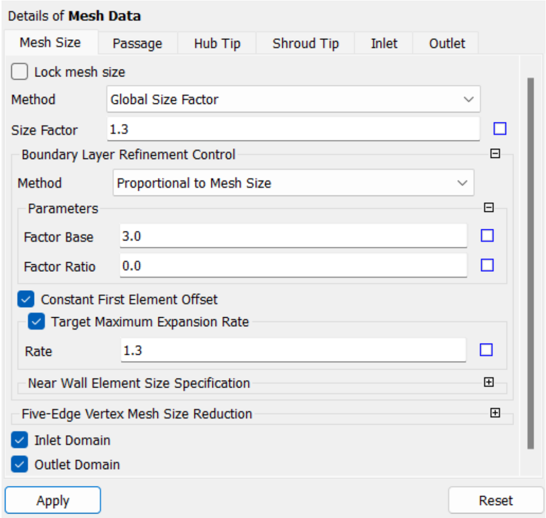

Details of **Mesh Data**

☐ Lock mesh size

Method: Global Size Factor

Size Factor: 1.3

Boundary Layer Refinement Control

Method: Proportional to Mesh Size

Parameters

Factor Base: 3.0

Factor Ratio: 0.0

☑ Constant First Element Offset

☑ Target Maximum Expansion Rate

Rate: 1.3

Near Wall Element Size Specification

Five-Edge Vertex Mesh Size Reduction

☑ Inlet Domain

☑ Outlet Domain

Figure 18. Mesh Data dialog box

3.2.3.2 No Tip Clearance Model

For the No Tip Clearance model, the tip clearance region was not included, resulting in a geometry where the blade extends completely to the shroud without a gap. Five different Global Size Factors (0.8, 0.9, 1.0, 1.1, and 1.2) were applied to investigate mesh independence and the default settings for the rest of the parameters.

3.3 Setup

This section focuses on the key elements involved in configuring a CFD simulation in Ansys CFX, including the specification of boundary conditions, selection of solver parameters, and setting appropriate convergence criteria. All setup procedures used were the same for the simulation with and without tip clearance.

The Turbo Mode feature in CFX-Pre was used as it is specifically designed for turbomachinery applications and streamlines the setup for simulating rotating machinery such as compressors, turbines and pumps. It provides tools and workflows tailored to rotating domains, including automatic handling of rotating reference frames and periodic boundary conditions. The analysis was conducted in a steady-state framework and the working fluid was specified as Air Ideal Gas with a reference absolute pressure of 0 atm. Heat transfer within the domain was modeled using the Total Energy approach.

3.3.1 Boundary Conditions

Defining boundary conditions in CFX is essential because they establish the physical constraints and flow conditions for the simulation, directly affecting both accuracy and stability. Boundary conditions determine how the fluid enters, exits, and interacts with surfaces within the domain, which is critical to replicating real-world behavior and achieving reliable results.

Boundary conditions in CFX can take several forms, depending on the application. Common types include inlet conditions, which are often defined by specifying total pressure and total temperature, or by setting a velocity profile. Outlet conditions can be specified using static pressure or mass flow. Wall conditions, such as non-slip walls for solid surfaces, capture the interaction between the fluid and the boundary, with options for specifying heat transfer when thermal effects are important. Additional types, such as symmetric, periodic, and rotating boundaries, allow for simplifications in geometry and complex rotating flows, improving computational efficiency.

In this study, the specific boundary conditions applied are listed in Table 3. The entire rotor region is defined as a rotating component with a rotational velocity of 16,043 rev/min. The inlet boundary condition is defined by a total temperature and total pressure, while the outlet boundary condition is defined by a mass flow rate. A no-slip condition is applied to all solid walls, and periodic boundary conditions are used to simulate the recurring nature of the flow around the rotor.

Table 3. Boundary conditions

Rotational velocity	16043 rev/min
Inlet total pressure	1 atm
Inlet total temperature	288 K
Outlet mass flow rate (per machine)	33.25 kg/s
Solid walls	No-slip Wall

The wall influence on flow for the shroud is defined as a counter-rotating wall as can be seen in Figure 19, which means the shroud surface moves in the opposite direction to the rotor's rotation. This setup represents the physical reality in high-speed compressors where the casing remains stationary relative to the rotating blades. All the other definitions have been left as the default.

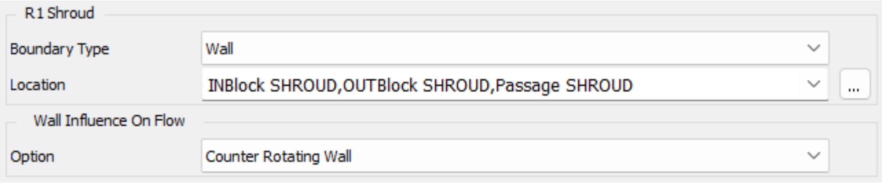

R1 Shroud

Boundary Type: Wall

Location: INBlock SHROUD,OUTBlock SHROUD,Passage SHROUD

Wall Influence On Flow

Option: Counter Rotating Wall

Figure 19. Boundary definition of Shroud wall

With the Turbo Mode setup completed, Figure 20 shows the computational domain configured accordingly.

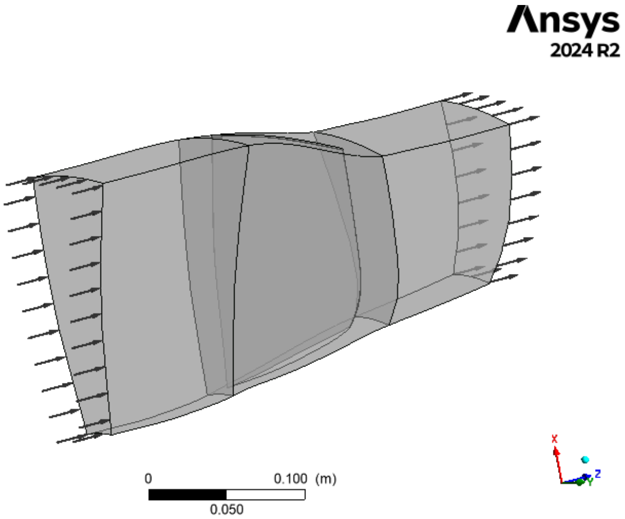

Figure 20. Computational Domain for NASA Rotor 67

3.3.2 Solver Control

In Ansys CFX, selecting the appropriate advection scheme is key to balancing accuracy and robustness in simulations. The Upwind scheme provides a first-order approach with high robustness, although it can lead to some numerical diffusion. The High-Resolution uses a more sophisticated method to calculate the fluxes, involving a combination of upwind and central difference schemes. It is more accurate in capturing sharp gradients but can be less stable in certain flow conditions. Alternatively, the Specified Blend Factor allows a user-defined blend between first and second-order schemes, enabling a balance between robustness and accuracy but risking overshoots at higher values and diffusivity at lower ones.

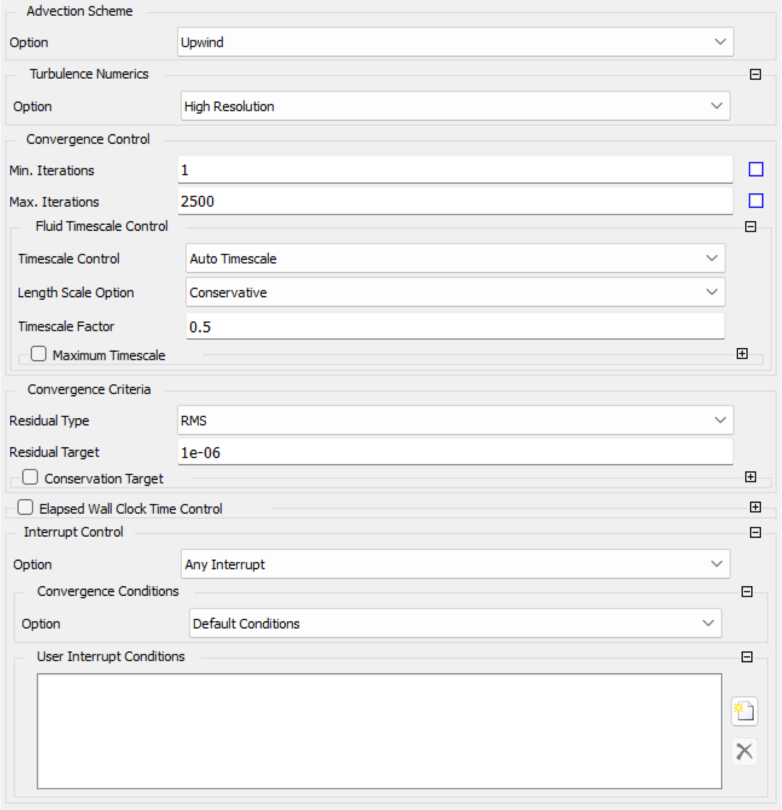

Advection Scheme
Option: Upwind
Turbulence Numerics
Option: High Resolution
Convergence Control
Min. Iterations: 1
Max. Iterations: 2500
Fluid Timescale Control
Timescale Control: Auto Timescale
Length Scale Option: Conservative
Timescale Factor: 0.5
☐ Maximum Timescale
Convergence Criteria
Residual Type: RMS
Residual Target: 1e-06
☐ Conservation Target
☐ Elapsed Wall Clock Time Control
Interrupt Control
Option: Any Interrupt
Convergence Conditions
Option: Default Conditions
User Interrupt Conditions

Figure 21. Basic settings of solver control

Figure 21 shows all parameters used in the simulation. Parameters not explicitly discussed are set to their default values.

The upwind advection scheme is used to ensure stability and prevent numerical oscillations in the solution. High resolution settings for the turbulence numerics were chosen to improve the accuracy of the turbulence predictions.

Convergence control in this study was managed by a combination of a maximum iteration limit and an RMS residual target to ensure solution stability and accuracy. The maximum number of iterations was set at $2{,}500$, with an RMS residual target of $1e-06$ to monitor the reduction of residuals over time.

A time scale factor of 0.5 was applied to stabilize the solution process by controlling the time step size, thus promoting convergence within the defined criteria. Although the analysis is steady-state, the solver iterates towards a final solution, and the time scale factor adjusts how aggressively flow variables are updated. A well-chosen value balances stability and convergence speed, preventing slow progress or numerical instability.

A pressure ratio output control monitor was also used to observe the ratio of outlet to inlet pressure, primarily to assess convergence. Monitoring this ratio provides insight into whether the simulation has stabilized to a final value or if fluctuations persist, indicating a need for further iterations.

3.3.3 SST Model

The k- ε and SST models are two of the most widely used turbulence models in CFD, each suitable for different flow conditions. The k-ε model is recognized as the industry standard for general purpose simulations due to its stability, robustness, and proven predictive capabilities, especially when combined with scalable wall functions for fine near-wall meshes. However, it can be less accurate for flows with separations, sudden strain changes, or rotating fluids. In contrast, the Shear-Stress Transport (SST) model is particularly well suited for predicting flow separation under unfavorable pressure gradients. By incorporating transport effects, it provides more conservative and accurate predictions for separated flows than standard two-equation models, making it a preferred choice for some applications.

The turbulence model used in the simulation was the Shear-Stress Transport (SST) model, which combines the advantages of the k-ω and k-ε models to provide accurate predictions of boundary layer turbulent flow. As shown in a Rotor 67 study in 2023 by W. Yan et al., the SST is more accurate in calculating and predicting the position of the shock wave when compared with other models. The performance curve is also slightly better than the other turbulence models used due to the hybrid form of k-ω and k-ε [23].

In the SST turbulence model, two key equations govern turbulence behavior: the turbulent kinetic energy (k) equation and the specific dissipation rate (ω) equation. The k equation describes the transport of turbulent energy, taking into account the generation and dissipation of turbulence in the flow. The ω equation, on the other hand, governs the rate at which turbulence is dissipated, providing important information about the scale of turbulent eddies. Together, these equations allow the SST model to simulate the complex behavior of turbulence. The turbulent kinetic energy equation and the specific dissipation rate equation are respectively [24]:

$$\frac{\delta(\rho k)}{\delta t}+\frac{\delta\left(\rho u_j k\right)}{\delta x_j}=G-\beta^*\rho\omega k+\frac{\delta}{\delta x_j}\left[(\mu+\sigma_k\mu_t)\frac{\delta k}{\delta x_j}\right] \quad (5)$$

$$\frac{\delta(\rho\omega)}{\delta t}+\frac{\delta\left(\rho u_j\omega\right)}{\delta x_j}=\frac{\gamma}{\nu_t}G-\beta\rho\omega^2+\frac{\delta}{\delta x_j}\left[(\mu+\sigma_\omega\mu_t)\frac{\delta\omega}{\delta x_j}\right]+2(1-F_1)\frac{\rho\sigma_{\omega 2}}{\omega}\frac{\delta k}{\delta x_j}\frac{\delta\omega}{\delta x_j} \quad (6)$$

where G is a production term of turbulent kinetic energy, β^*, σ_k, γ, β, σ_ω and $\sigma_{\omega 2}$ are empirical coefficients and F_1 is a blending function that controls the transition between the k-ω model near walls and the k-ε model in the free stream.

3.4 Solution

As the simulation runs, it's important to monitor the simulation for signs of divergence, such as sudden spikes in residuals, oscillating values in output monitors, or failure to reach convergence criteria within a reasonable number of iterations. These indicators can signal problems such as inappropriate boundary conditions, excessively large time steps, or numerical instabilities. Adjustments to parameters such as time scale, mesh quality, or solver settings may be necessary to ensure stability and guide the simulation toward accurate, stable results.

A converged solution does not always guarantee accuracy, since convergence only indicates that the solution has stabilized according to certain numerical criteria. Even with small residuals, the solution may be physically incorrect. Therefore, validation against expected physical behavior, experimental data, or theoretical results is essential to ensure that a converged solution accurately represents the real-world scenario.

3.5 Results

The CFX Results module provides comprehensive tools for analyzing and visualizing the simulation outcomes, allowing users to evaluate flow characteristics, performance metrics, and convergence behavior in detail.

Through a variety of post-processing options such as contour plots, vector fields, and quantitative reports, the Results module helps to interpret complex flow phenomena and identify regions of interest such as pressure gradients and turbulent zones, and validate the simulation against expected physical behavior.

CHAPTER 4 – RESULTS

4.1 Mesh Independence

4.1.1 Tip Clearance Model

Table 4 illustrates the effect of mesh refinement on the pressure ratio of the simulation with the tip clearance, with various Global Size Factors (GSF) showing a trend toward convergence as the mesh becomes finer.

Starting with GSF equal to 0.8, which has a significant relative error of 0.840%, each increase in GSF results in a denser mesh and a lower relative error, indicating improved accuracy. When the GSF reaches 1.2, the pressure ratio stabilizes with a relative error of 0.099%, less than 0.1%, indicating that further refinement offers negligible change in accuracy.

Therefore, the mesh corresponding to GSF 1.2 was selected as the final mesh for the simulation with the tip clearance because it balances computational efficiency with high solution accuracy.

Table 4. Tip clearance mesh independence study

Global Size Factor	Mesh Nodes	Mesh Elements	Pressure Ratio	Relative Error
GSF 0.8	128306	118208	1,6325	0.840%
GSF 1.0	247076	231405	1,6189	0.509%
GSF 1.2	460352	436708	1,6107	0.099%
GSF 1.3	554182	527446	1,6091	0.050%
GSF 1.4	725694	693780	1,6083	-

Note that, in Table 4, the values in the 'Relative Error' column are calculated relative to the finer mesh, using the following equation:

$$Relative\ Error_i\ [\%] = \left(\frac{PR_i - PR_{i+1}}{PR_{i+1}}\right) \times 100 \quad (7)$$

where PR_i is the pressure ratio for mesh i and PR_{i+1} is the pressure ratio for the next mesh.

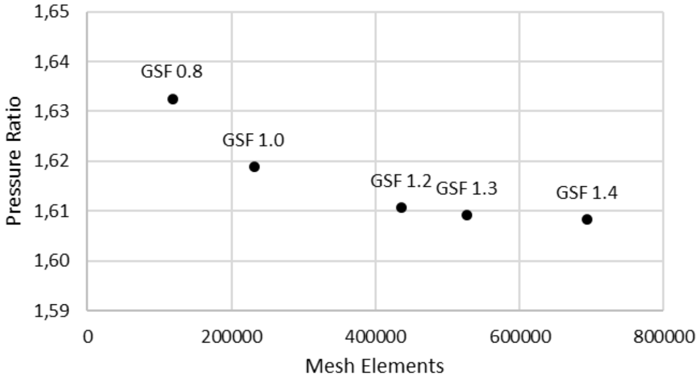

Figure 22. Pressure ratio for different meshes

The pressure ratio and number of mesh elements are plotted in Figure 22 to provide a clearer visual representation of their variation.

4.1.2 No Tip Clearance Model

Table 5 illustrates the effect of mesh refinement on the pressure ratio of the simulation with the tip clearance, with various Global Size Factors (GSF) showing a trend toward convergence as the mesh becomes finer.

Starting with GSF equal to 0.8, which has a significant relative error of 0.306%, each increase in GSF results in a denser mesh and a lower relative error, indicating improved accuracy. When the GSF reaches 1.1, the pressure ratio stabilizes with a relative error of 0.083%, less than 0.1%, indicating that further refinement offers negligible change in accuracy.

Therefore, the mesh corresponding to GSF 1.1 was selected as the final mesh for the simulation without the tip clearance because it balances computational efficiency with high solution accuracy.

Table 5. No Tip Clearance Mesh Independence Study

Global Size Factor	Mesh Nodes	Mesh Elements	Pressure Ratio	Relative Error
GSF 0.8	90420	82795	1.7046	0.306%
GSF 0.9	119559	110336	1.6994	0.266%
GSF 1.0	167721	156204	1.6949	0.225%
GSF 1.1	227263	213200	1.6911	0.083%
GSF 1.2	286560	270116	1.6897	-

Note that in Table 5, the values in the 'Relative Error' column are calculated relative to the finer mesh, using equation (7).

The pressure ratio and number of mesh elements are plotted in Figure 23 to provide a clearer visual representation of their variation.

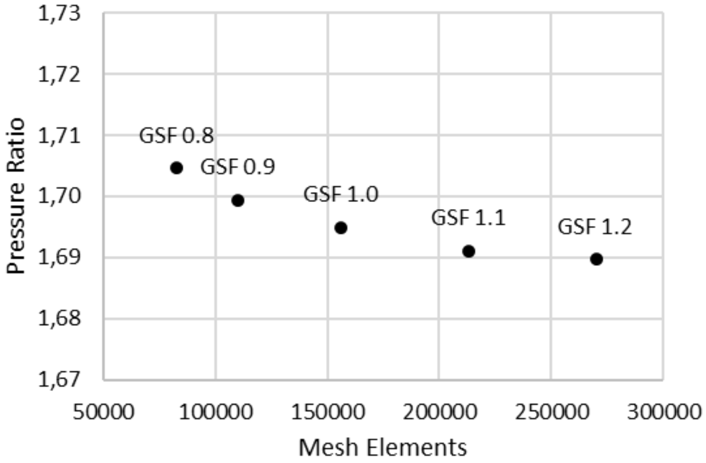

Figure 23. Pressure ratio for different meshes

4.2 Mesh Quality

In this section, the quality of the mesh will be evaluated according to the metrics described previously to ensure that it meets the required standards for accuracy and stability in the simulations. Those metrics are orthogonal angle and skewness.

4.2.1 Tip Clearance Model

For the tip clearance model, the mesh orthogonality angle histogram (Figure 24) indicates that all elements meet the required minimum angle of 20°, ensuring compliance with quality standards. Furthermore, the mesh demonstrates a high overall quality, with an average orthogonality angle of 79.1°.

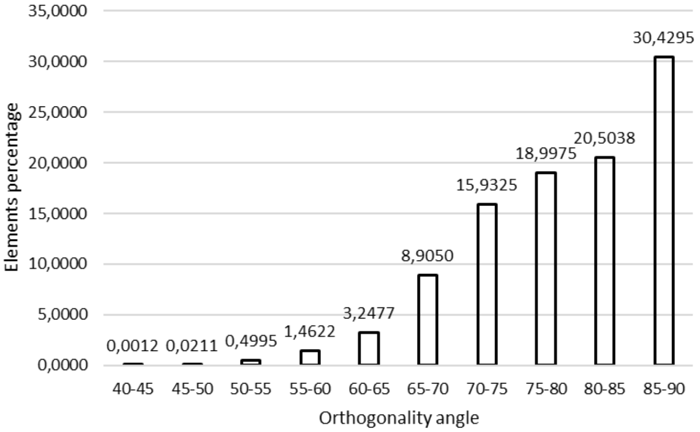

Figure 24. Mesh orthogonality angle histogram

As for the mesh skewness, the histogram in Figure 25 shows that approximately 99.87% of the elements fall into the excellent or good quality categories, according to the previously defined standards. The remaining elements are classified as fair or poor; however, their small proportion is negligible and won't have a significant impact on the overall simulation results. In addition, the mesh has an average skewness value of 0.1573.

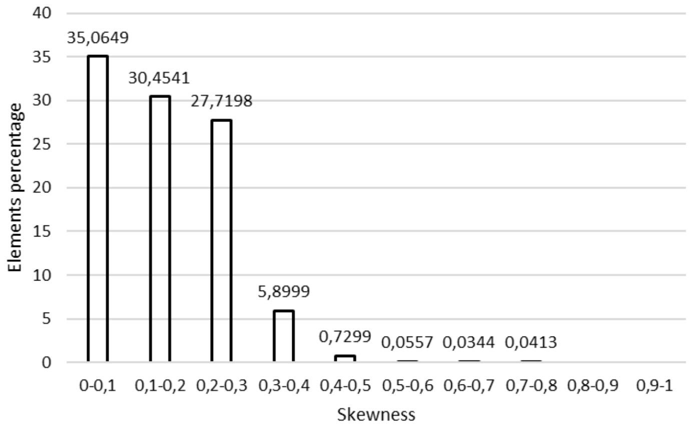

Figure 25. Mesh skewness histogram

4.2.2 No Tip Clearance

In the case of no tip clearance, the mesh orthogonality angle also exceeds the minimum of 20° for all elements, as can be seen in Figure 26, ensuring compliance with the quality criteria. The average orthogonality angle for this configuration is 76.3°.

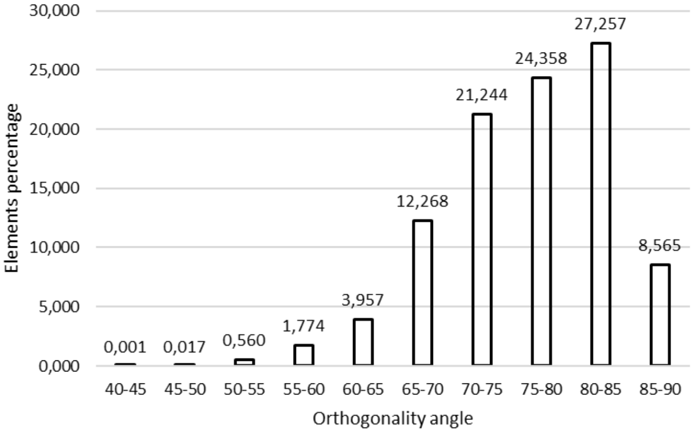

Figure 26. Mesh orthogonality angle histogram

In this model, the mesh skewness analysis shows that approximately 99.97% of the elements are classified as excellent or good based on the previously defined quality standards, as it can be checked in Figure 27. The remaining elements fall into the fair category. The average skewness value is 0.1878.

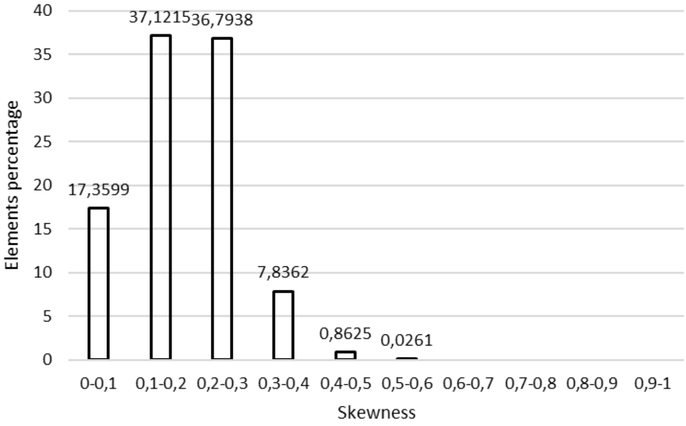

Figure 27. Mesh skewness histogram

4.3 Model Validation

In this validation section, the simulation results are compared to experimental data from NASA Technical Report, Laser anemometer measurements in a transonic axial-flow fan rotor [10] to assess the accuracy and reliability of the model. Two key performance metrics are analyzed: pressure ratio and efficiency as a function of normalized mass flow.

The total pressure ratio is defined as the ratio of the total (stagnation) pressure at the outlet (P_{t2}) to the total pressure at the inlet (P_{t1}):

$$Total\ pressure\ ratio = \frac{P_{t2}}{P_{t1}} \quad (8)$$

As for efficiency, it is expressed as the ratio of the work output from an ideal, isentropic compression process to the actual work input required:

$$Efficiency = \frac{\left(\frac{P_{t2}}{P_{t1}}\right)^{\frac{\kappa-1}{\kappa}} - 1}{\frac{T_{t2}}{T_{t1}} - 1} \quad (9)$$

where P_{t1} and P_{t2} are inlet and outlet stagnation pressures, T_{t1} and T_{t2} are inlet and outlet stagnation temperatures and κ is the ratio of specific heats.

This comparison is essential to confirm that the simulation parameters and boundary conditions accurately represent the real-world performance of the compressor rotor.

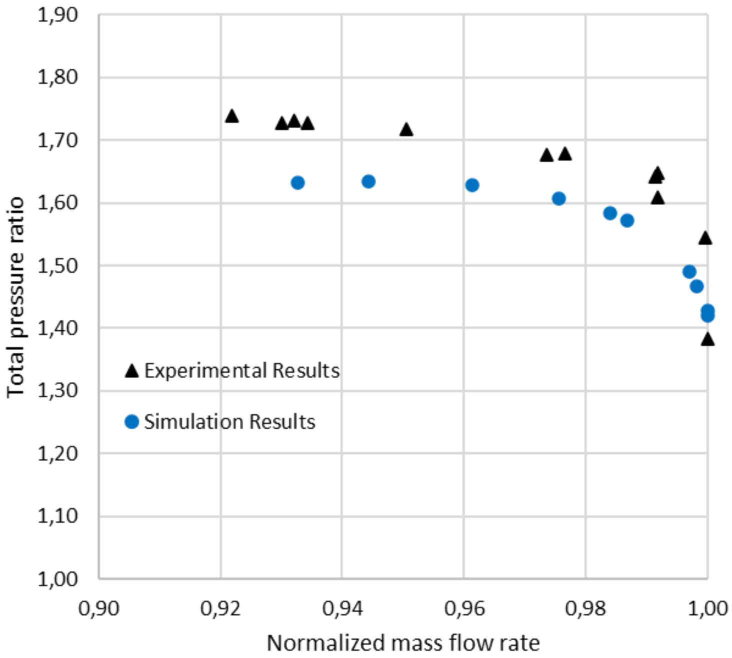

Figure 28. Total pressure ratio variation with mass flow: simulation and experimental results

Looking at Figure 28 and Figure 29, although the simulation points do not perfectly match the experimental values, both show similar overall trends for the characteristics studied. The simulated values are slightly lower than the experimental values over the entire range.

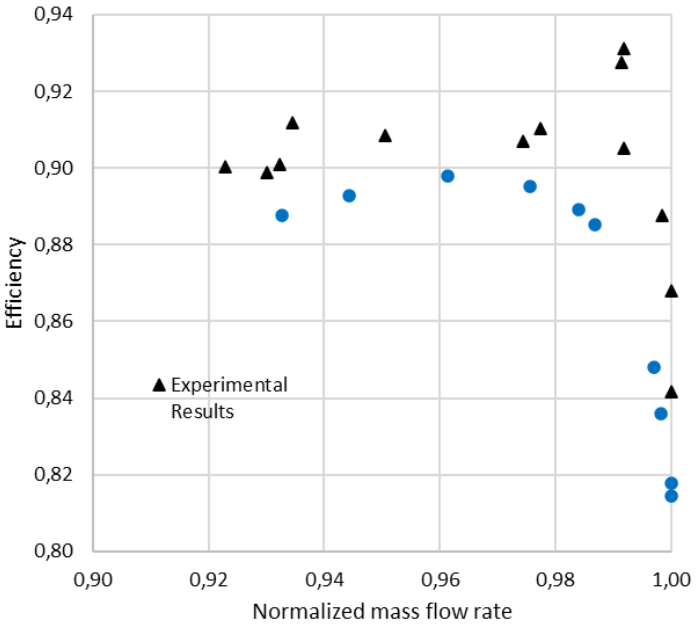

Figure 29. Efficiency variation with mass flow: simulation and experimental results

For the efficiency graph, the simulation does not capture the peak observed in the experimental results. Despite this difference, the agreement in trends allows the model to be considered valid, as it effectively represents the overall behavior of the system.

In addition to the graphs, Table 6 is provided with key values such as the choke mass flow rate, and design pressure ratio, along with their relative errors when compared to the experimental results.

Table 6. Comparison between experimental and simulation results

	Experimental	**Simulation**	**Relative error**
Choke mass flow rate	34.96 kg/s	34.35 kg/s	1.74 %
Design pressure ratio	1.63	1.57	3.50 %

Choked mass flow occurs when a gas flows through a narrow passage and reaches the speed of sound at the smallest cross-section. Once this happens, the mass flow remains constant no matter how much the downstream pressure decreases.

In this study, choking was identified by the mass flow to pressure ratio. If the total pressure ratio continues to decrease and the mass flow does not change, choking has occurred as can be observed in Figure 29.

4.4 Tip Clearance Model

This section presents the results of the tip clearance simulation, including an analysis of key performance metrics and visual representations of the flow behavior. Several contour plots generated in CFX Post are included to provide a clearer understanding of the effects of tip clearance on rotor performance.

Figure 30 shows the residuals from the simulation, illustrating the convergence behavior over iterations. The simulation successfully converged to the objective target RMS residual of 1e-06, requiring 727 iterations.

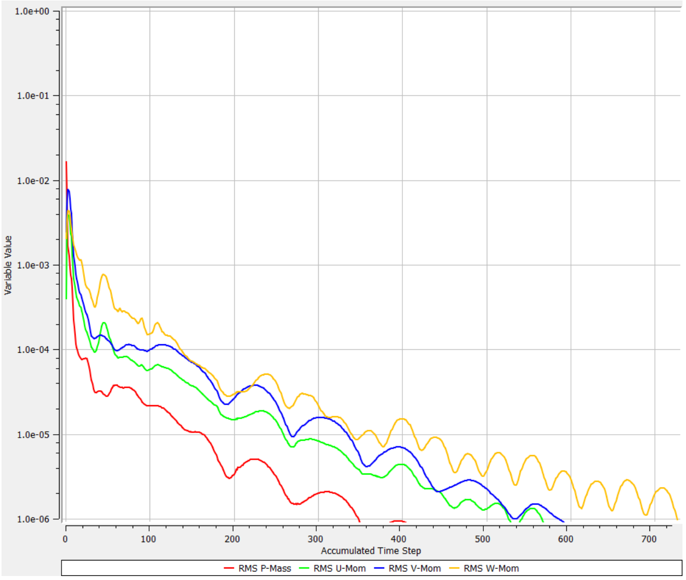

Figure 30. Residuals convergence for the simulation

Figure 31a shows the relative Mach number contour on a meridional surface section, with the flow entering from the left.

Before the flow reaches the blade, there is a noticeable increase in velocity from the hub to the shroud. A shock wave in the passage is indicated by the relative Mach increasing and then decreasing. The streamwise plot (Figure 32) clearly shows the shock wave beginning at the streamwise location 0.45.

The pressure contour (Figure 31b) shows a clear rise from the inlet to the outlet. A low-pressure region (dark blue) is visible at the leading edge of the blade, caused by the interaction with the blade, which reduces the static pressure in this area. Downstream, the pressure increases significantly (green to orange colors), reflecting compression by the rotor.

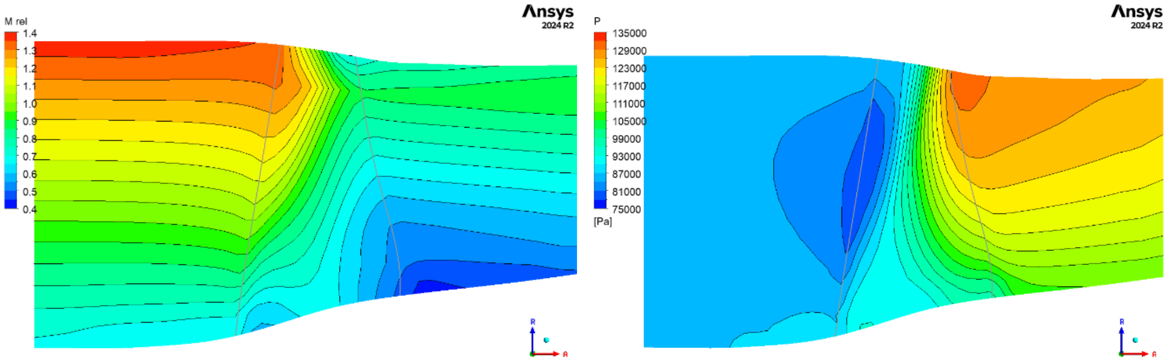

(a) **(b)**

Figure 31. Meridional surface contours: (a) relative mach; (b) pressure

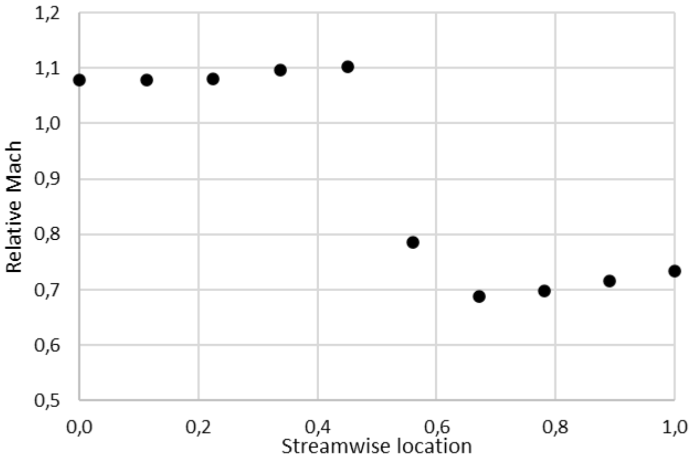

Figure 32. Streamwise plot of relative Mach number

Figure 33 shows the relative Mach contour at different blade spans: 20%, 50% and 80% respectively. Each graph highlights the flow behavior near the hub, mid-span, and blade tip, including the formation of leading-edge shock waves and how their intensity changes along the blade span.

At 20% span, corresponding to the region near the hub, the relative Mach number is lower and the leading-edge shock waves appear weaker and more diffuse. This is due to the reduced flow acceleration and the influence of secondary flow effects and boundary layers near the hub, which reduce the intensity of the flow.

At 50% span, the center of the blade, the relative Mach number increases and the leading-edge shockwaves become stronger and more pronounced. Note that this region is often the most aerodynamic efficient.

At 80% span, near the blade tip, the leading-edge shock waves are most intense. The contours show sharp and well-defined shock structures corresponding to the high relative Mach numbers typical of this region. The higher speed near the tip amplifies the relative flow velocity. Tip leakage flow adds to the complexity of the flow near the tip.

Figure 34a shows a general view of the relative Mach number near the trailing edge of the blades. It can be seen how the contour changes from the hub to the tip, with the Mach number increasing along the span. Near the hub, the flow exhibits smoother gradients, while near the tip, the Mach number distribution becomes sharper and more uneven.

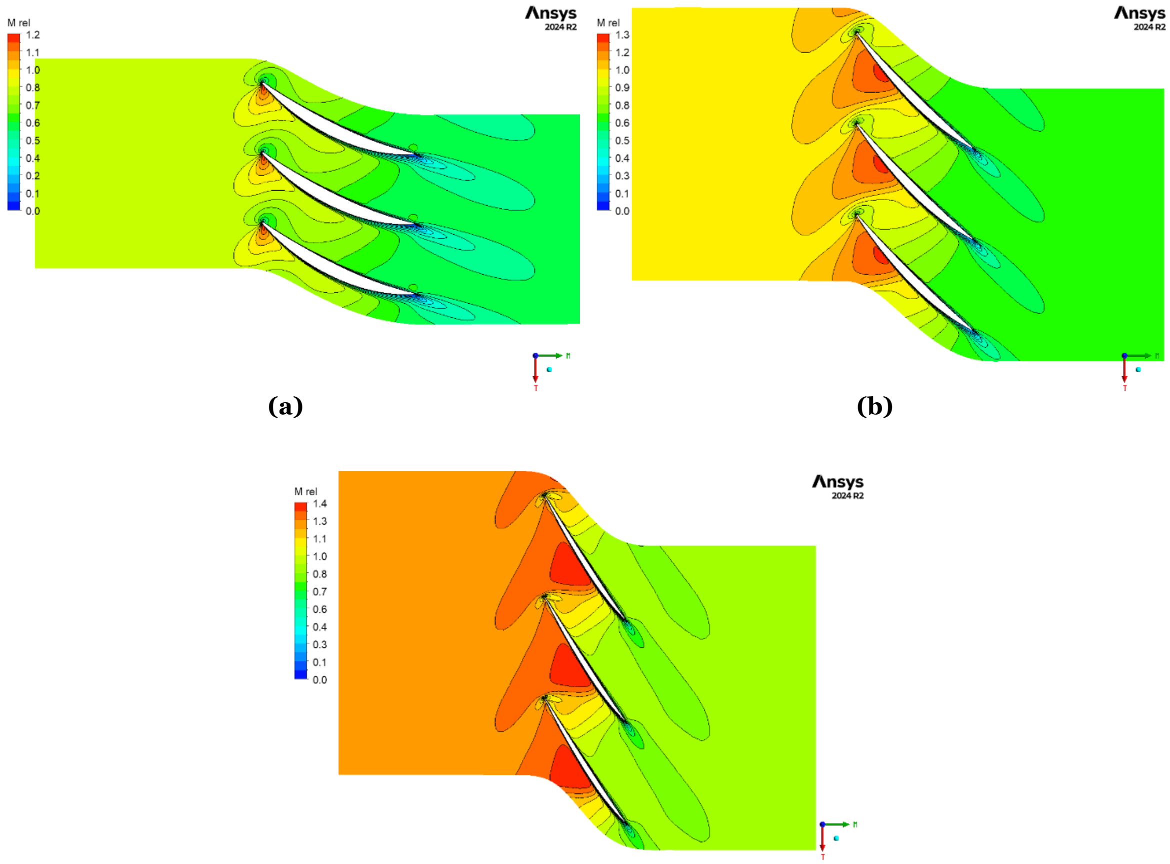

(a) (b)

(c)

Figure 33. Relative Mach contour at different blade spans: (a) 20%; (b) 50%; (c) 80%

Figure 34b focuses on the trailing edge near the tip, highlighting the effects of tip clearance. The flow is more complex, with high gradients caused by tip leakage, where air escapes over the blade tip from the pressure side to the suction side. This creates a vortex, visible in the distorted Mach number contours, which adds losses and turbulence to the flow.

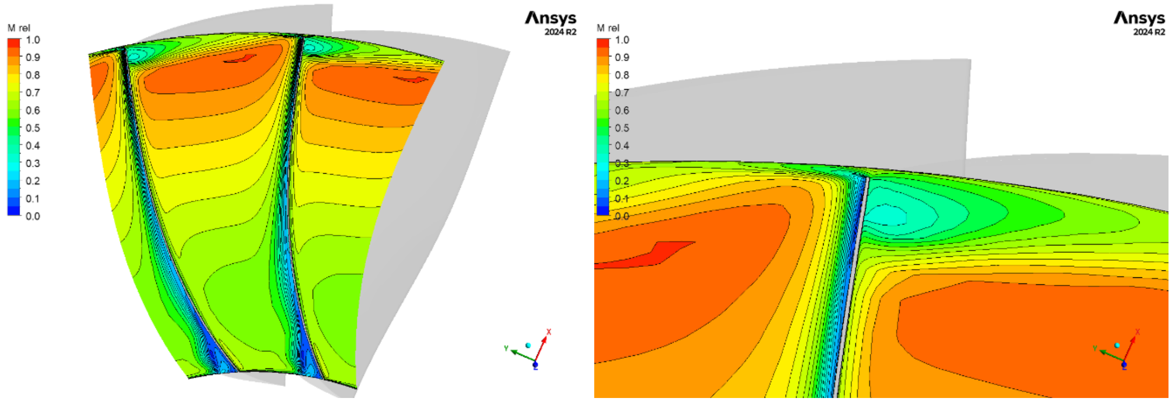

(a) (b)

Figure 34. Relative Mach contour at trailing edge: (a) general view; (b) tip clearance close-up

Figure 35 shows the pressure contour at the trailing edge. This contour shows a gradual increase in pressure from the hub to the tip. Near the hub, the pressure is lower, with smooth contours indicating stable aerodynamic behavior.

Closer to the tip, the pressure gradient shows significant irregularities. These are caused by the leak flow perturbing the pressure field and forming a leak vortex at the tip.

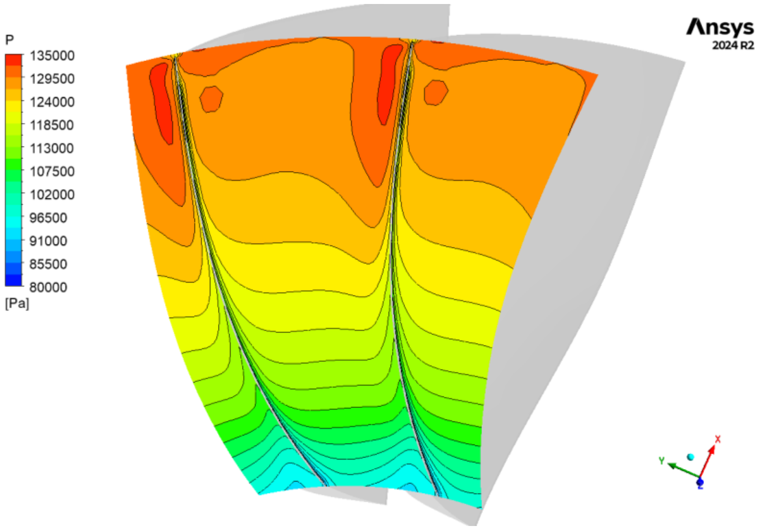

Figure 35. Pressure contour at trailing edge cut

Figure 36 shows a noticeable deviation in streamline behavior near the tip of the blade. The clearance allows leakage flow to develop, creating secondary flow structures that interact with the main flow. This interaction distorts the streamlines near the tip region. The increased complexity of the flow pattern indicates additional aerodynamic losses due to mixing and vortex generation in the tip clearance region.

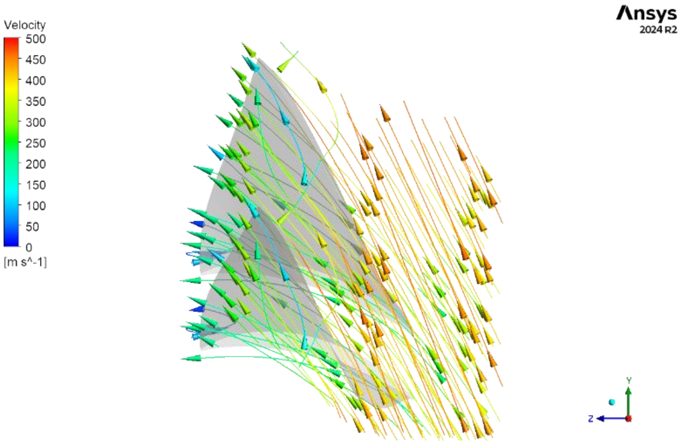

Figure 36. Velocity streamlines

4.5 No Tip Clearance Model

Figure 37 shows the residuals from the simulation, illustrating the convergence behavior over iterations. The simulation successfully converged to the objective target RMS residual of 1e-06, requiring 937 iterations.

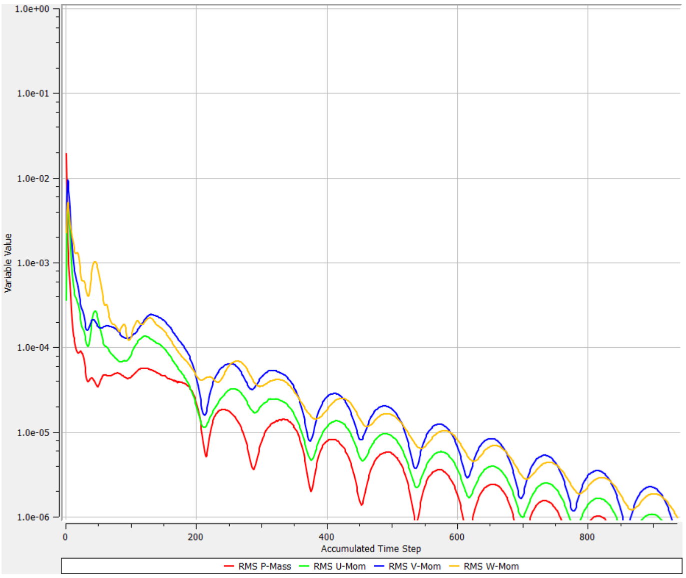

Figure 37. Residuals convergence for the simulation

Figure 38a shows the relative Mach number contour on a meridional surface section, with the flow entering from the left.

Before the flow reaches the blade, there is a noticeable increase in velocity from the hub to the shroud. A shock wave in the passage is indicated by the relative Mach increasing and then decreasing. The streamwise plot (Figure 39) shows the shock wave beginning at around streamwise location 0.45.

The pressure contour (Figure 38b) shows a clear rise from the inlet to the outlet. A low-pressure region (dark blue) is visible at the leading edge of the blade, caused by the interaction with the blade, which reduces the static pressure in this area. Downstream, the pressure increases significantly (green to orange colors), reflecting compression by the rotor.

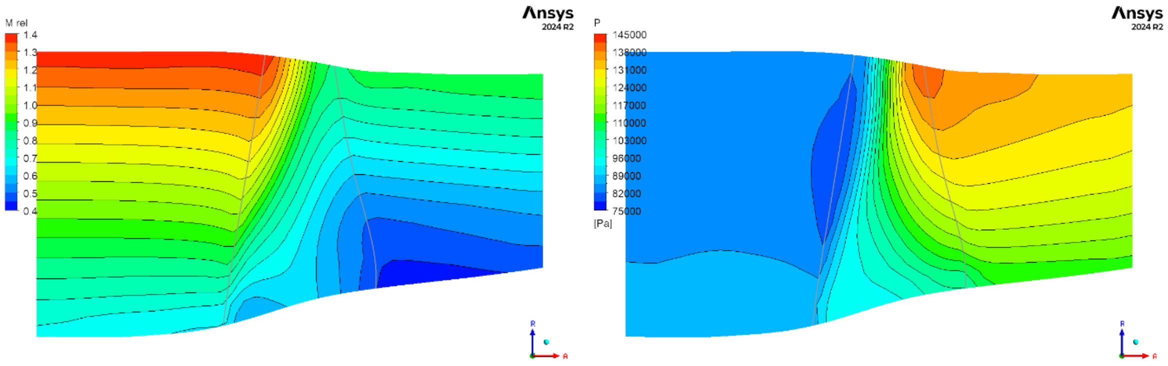

(a) **(b)**

Figure 38. Meridional surface contours: (a) relative Mach; (b) pressure

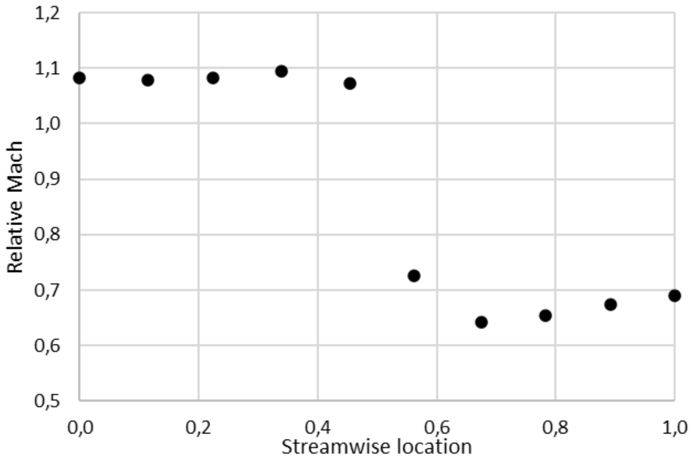

Figure 39. Streamwise plot of relative Mach number

Figure 40 shows the relative Mach number contour at different blade spans: 20%, 50%, and 80%, to illustrate the flow behavior from the hub to the tip.

At 20% span, near the hub, the relative Mach number is lower, and the leading-edge shock waves are weaker and more diffuse due to reduced flow acceleration and boundary layer effects.

At 50% span, the center of the blade, the relative Mach number increases and the leading-edge shockwaves become stronger and more pronounced.

At 80% span, near the tip, the relative Mach number is highest, with sharp and well-defined leading-edge shocks caused by the high relative velocities in this region. In the absence of tip clearance, the flow near the tip is less complex, as tip leakage effects are eliminated, resulting in a reduced wake.

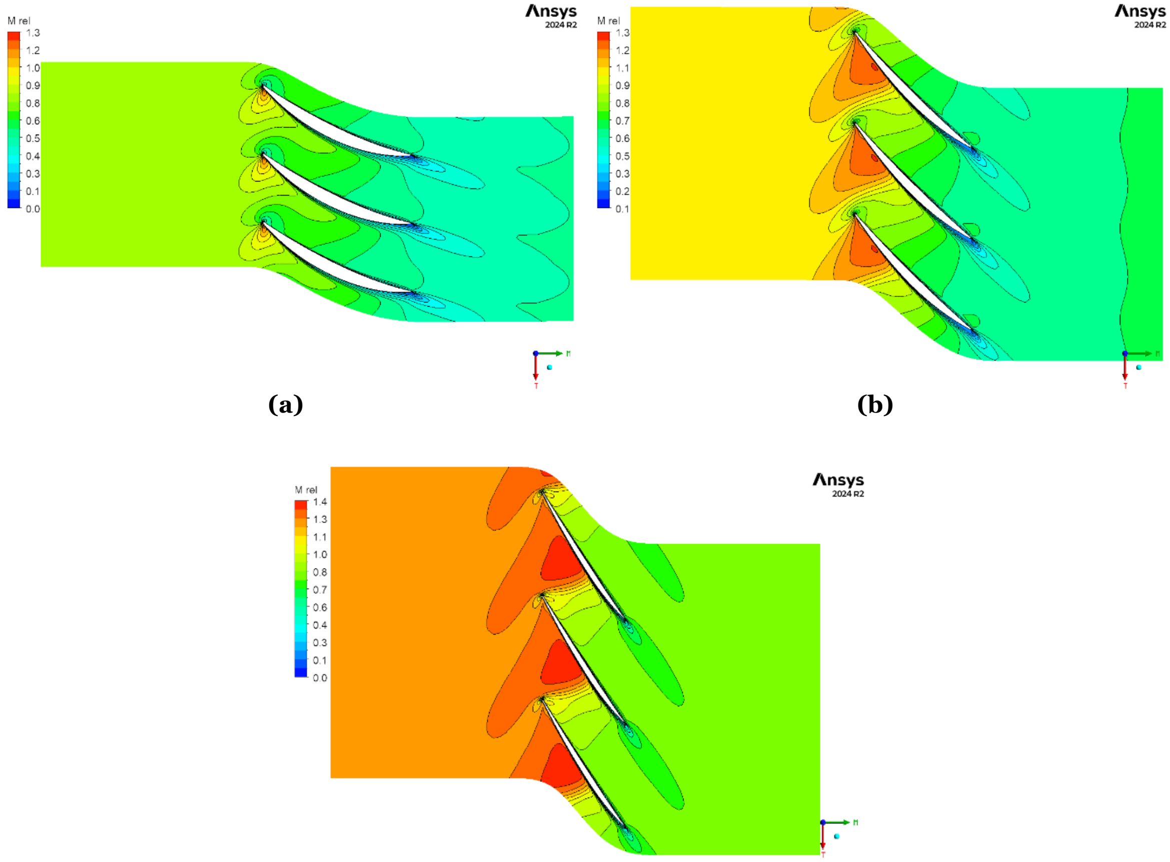

(a) **(b)**

(c)

Figure 40. Relative Mach contour at different blade spans: (a) 20%; (b) 50%; (c) 80%

Figure 41a shows a general view of the relative Mach number near the trailing edge of the blades. The contour changes from the hub to the tip, with the Mach number increasing along the span. Although there are variations in the Mach number distribution, they are less pronounced, indicating a more uniform flow near the trailing edge.

Figure 41b focuses on the blade and shroud interaction for the model with no tip clearance. The flow appears more stable, with fewer irregularities and less distortion in the Mach number contours. In the absence of tip clearance, flow from the pressure side to the suction side is suppressed, reducing turbulence and minimizing losses in this region.

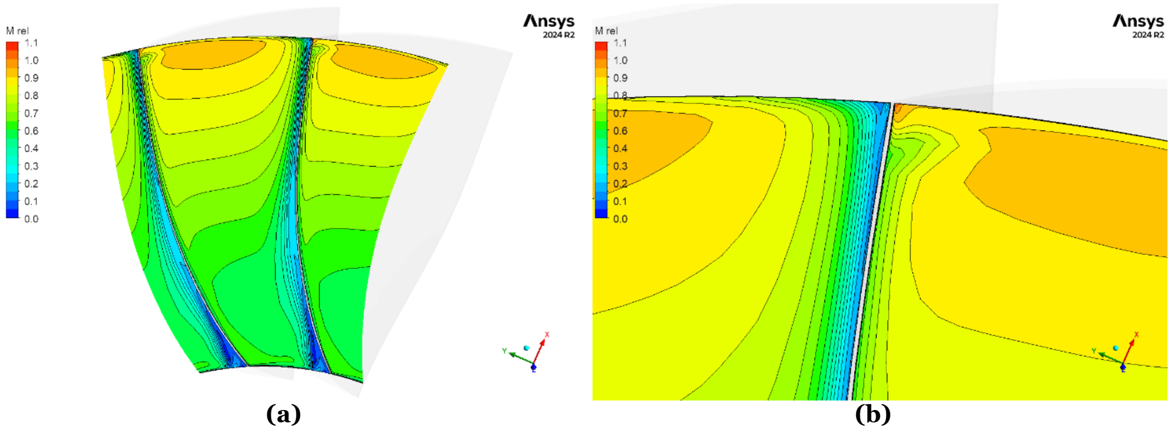

Figure 41. Relative Mach contour at trailing edge: (a) general view; (b) tip close-up

Figure 42 shows the pressure contour at the trailing edge. This contour reveals a gradual increase in pressure from the hub to the tip. Near the hub, the pressure is lower, with smooth contours indicating stable aerodynamic behavior.

Closer to the tip, the pressure gradient remains more uniform and stable compared to models with tip clearance. The absence of leak flow eliminates the perturbation in the pressure field, resulting in a smoother pressure distribution and reducing flow irregularities near the blade tip.

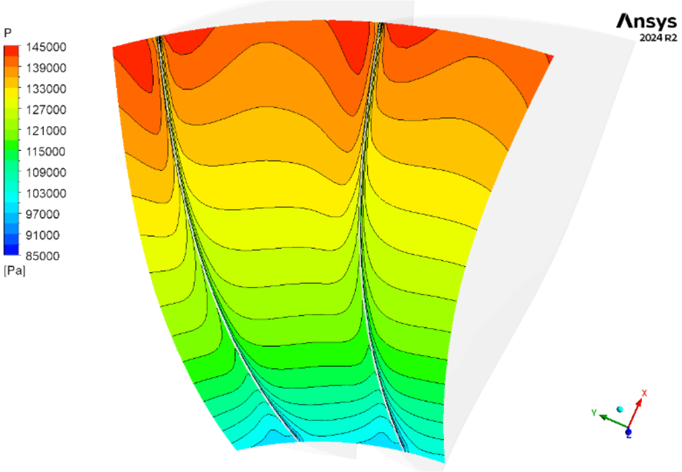

Figure 42. Pressure contour at trailing edge cut

Figure 43, which shows the velocity streamlines for the simulation without tip clearance, shows that the streamlines remain well organized as they pass through the rotor. The absence of clearance eliminates leakage flow, allowing the main passage flow to remain more uniform and closely aligned with the blade surfaces. This results in a more controlled streamline pattern, which contributes to improved aerodynamic efficiency.

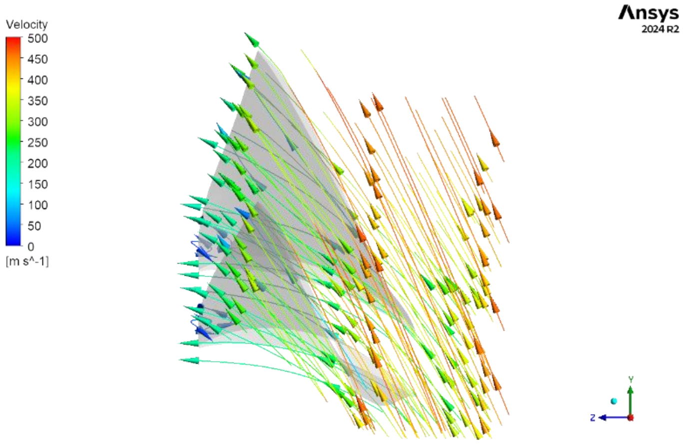

Figure 43. Velocity streamlines

4.6 Model Comparison

As shown in Table 7, the rotor with no tip clearance performs better. Without the gap, the flow remains more streamlined as can be seen by comparing Figure 36 and Figure 43, improving pressure and temperature ratios, while also improving efficiency by eliminating the turbulence and flow separation that occurs with tip clearance. These factors result in more efficient compression and more stable flow across the blades, resulting in higher overall performance.

Table 7. Performance characteristics of rotor with and without tip clearance

	Tip clearance	No tip clearance
Pressure ratio	1,611	1,691
Temperature ratio	1,167	1,180
Efficiency	88,41 %	90,23 %

The images presented in the previous sections illustrate why the performance is superior in the model without tip clearance. As seen, the flow dynamics in the model without the clearance result in more favorable pressure and Mach distributions. For example, comparing Figure 34b and Figure 41b, in the case of tip clearance, the flow near the trailing edge is disrupted by leakage, creating a wider and less defined wake. This results in higher aerodynamic losses and reduced performance. In the second case, with no tip clearance, the flow is more uniform, indicating less energy dissipation and better efficiency due to the absence of leakage effects.

In Figure 31a and Figure 38a, it is also evident that along the trailing edge, from the hub to the shroud, the relative Mach increases gradually from 0.4 to about 0.9 in the case of the model without tip clearance. However, in the model with tip clearance, it increases from

0.4 to about 0.9, but begins to decrease near the blade tip, reaching about 0.7. This could be attributed to the interaction with the flow passing through the clearance.

This can also be observed in Figure 39 and Figure 42. For the rotor without tip clearance, the pressure reached is higher, around 145,000 Pa compared to 135,000 Pa for the rotor with tip clearance. Additionally, near the blade tip, the contours are noticeably more irregular in the case with tip clearance.

CHAPTER 5 – CONCLUSION

5.1 Conclusion

This study focused on a comparative analysis of two configurations of the NASA Rotor 67: one with tip clearance and the other without. The objective was to assess the impact of tip clearance on the aerodynamic performance of the rotor, specifically under transonic flow conditions. Using Ansys CFX, simulations were performed to capture the flow behavior and quantify changes in key performance parameters, such as pressure, Mach number, and overall flow structure. These parameters were evaluated at critical locations, including the blade tip, to better understand the effects of clearance on rotor efficiency and performance.

The results demonstrated clear and significant differences between the two configurations. In the model without tip clearance, the pressure distribution exhibited higher values, reaching approximately 145,000 Pa, compared to the 135,000 Pa observed in the model with tip clearance. This difference can be attributed to the elimination of flow leakage through the clearance gap, which reduces pressure loss and contributes to improved aerodynamic efficiency. Without leakage, the flow remains more effectively guided by the blade surfaces, leading to better pressure recovery and higher performance.

The relative Mach contours further revealed smoother and more uniform flow behavior in the configuration without tip clearance. Across the blade span, particularly from the hub to the shroud, the relative Mach number increased gradually, reaching approximately 0.9 at the blade tip. This gradual increase suggests a stable acceleration of the flow along the blade surface, consistent with the expected aerodynamic behavior for well-designed transonic rotors. The absence of disturbances near the blade tip indicates minimal energy loss, which translates into enhanced efficiency.

Conversely, the rotor with tip clearance displayed notable irregularities in the flow near the blade tip. Although the relative Mach number initially followed a similar trend, rising to approximately 0.9, it subsequently declined to around 0.7 near the shroud. This reduction is indicative of the complex interactions passing through the clearance gap. The leakage flow creates local recirculation and vortices, which disrupt the flow near the tip and lead to flow separations and energy dissipation. These effects are clearly observed in the Mach contours, where regions of flow deceleration and irregularities become more pronounced closer to the tip. Such disturbances negatively impact the aerodynamic loading on the blade and result in a reduction in overall performance.

The findings of this study highlight the importance of minimizing tip clearance in transonic rotors to achieve a better aerodynamic performance. By reducing leakage flow, it is possible to maintain higher pressure rise, smoother flow acceleration, and reduced energy losses near critical blade regions. The results provide valuable insight for the design and optimization turbomachinery, where even minor improvements in efficiency can lead to significant gains in overall system performance.

5.2 Future Works

Future work could involve studying how different rotor designs affect the performance of axial compressors. For example, examining designs with different gaps could reveal further performance improvements and loss reduction mechanisms. Additionally, investigating varying operational conditions, including different rotational speeds, inlet temperatures, and flow rates outside of the design point, could provide a more comprehensive understanding of the compressor's behavior. Such studies would be beneficial for optimizing compressor performance across a wider range of conditions.

BIBLIOGRAPHY

[1] Rolls Royce, *The Jet Engine*. Derby: Rolls Royce plc, 1986.

[2] H. Cohen, *Gas Turbine Theory*. New York: Pearson, 1972.

[3] NASA GRC, “Ideal Brayton Cycle.” Accessed: Apr. 08, 2024. [Online]. Available: https://www.grc.nasa.gov/www/k-12/airplane/brayton.html

[4] NASA GRC, “Compressors.” Accessed: Mar. 06, 2024. [Online]. Available: https://www.grc.nasa.gov/www/k-12/airplane/compress.html

[5] Seppo A. Korpela, *Principles of Turbomachinery*. New Jersey: John Wiley & Sons, Inc., 2011.

[6] Meherwan P. Boyce, *Gas Turbine Engineering Handbook*. Houston: Gulf Professional Publishing, 1982.

[7] M. Righi, V. Pachidis, L. Könözsy, and L. Pawsey, “Three-dimensional through-flow modelling of axial flow compressor rotating stall and surge,” *Aerosp Sci Technol*, vol. 78, pp. 271–279, Jul. 2018, doi: 10.1016/j.ast.2018.04.021.

[8] Z. Xinqian and L. Anxiong, “Experimental investigation of surge and stall in a high-speed centrifugal compressor,” *J Propuls Power*, vol. 31, no. 3, pp. 815–825, Feb. 2015, doi: 10.2514/1.B35448.

[9] J. L. Kerrebrock, “Flow in transonic compressors,” *AIAA Journal*, vol. 19, no. 1, pp. 4–19, 1981, doi: 10.2514/3.50919.

[10] A. J. Strazisar, J. R. Wood, M. D. Hathaway, and K. L. Suder, “NASA Laser Anemometer Measurements in a Transonic Axial-Flow Fan Rotor,” 1989.

[11] P. Song and J. Sun, “Blade shape optimization for transonic axial flow fan,” *Journal of Mechanical Science and Technology*, vol. 29, no. 3, pp. 931–938, Mar. 2015, doi: 10.1007/s12206-015-0207-x.

[12] N. Z. Huang, X. Zhao, Y. H. Zhang, and X. Y. Wu, “Aerodynamic performance improvement of a transonic axial compressor by swept and leaned rotors,” in *AIAA Propulsion and Energy Forum and Exposition*, 2019. doi: 10.2514/6.2019-3819.

[13] J. H. Kim, K. J. Choi, and K. Y. Kim, “Aerodynamic analysis and optimization of a transonic axial compressor with casing grooves to improve operating stability,” *Aerosp Sci Technol*, vol. 29, no. 1, pp. 81–91, Aug. 2013, doi: 10.1016/j.ast.2013.01.010.

[14] C.-T. Dinh and K.-Y. Kim, “Effects of Air Injection on Aerodynamic Performance of a Single-Stage Transonic Axial Compressor,” *Design, Construction, Maintenance*, vol. 1, pp. 24–32, Mar. 2021, doi: 10.37394/232022.2021.1.4.

[15] M. Mohsen and M. M. E. Eg, “The Impact of Tandem Rotor Blades on the Performance of Transonic Axial Compressors,” *Aerosp Sci Technol*, vol. 67, pp. 237–248, Aug. 2017, doi: 10.1016/j.ast.2017.04.019.

[16] S. N. Danish *et al.*, “Effect of tip clearance and rotor-stator axial gap on the efficiency of a multistage compressor,” *Appl Therm Eng*, vol. 99, pp. 988–995, Apr. 2016, doi: 10.1016/j.applthermaleng.2016.01.132.

[17] S. S. Kumar *et al.*, “Aerodynamic characterization of a transonic axial flow compressor stage – with asymmetric tip clearance effects,” *Aerosp Sci Technol*, vol. 82–83, pp. 272–283, Nov. 2018, doi: 10.1016/j.ast.2018.09.001.

[18] T. Liang, B. Liu, S. Spence, X. Mao, and H. Cheng, “Numerical investigation into the effects of tip clearance on the performance of a counter-rotating axial flow compressor,” *Journal of Applied Fluid Mechanics*, vol. 13, no. 5, pp. 1587–1599, 2020, doi: 10.36884/JAFM.13.05.31177.

[19] B. Zhang, X. Mao, X. Wu, and B. Liu, “Effects of tip leakage flow on the aerodynamic performance and stability of an axial-flow transonic compressor stage,” *Energies (Basel)*, vol. 14, no. 14, Jul. 2021, doi: 10.3390/en14144168.

[20] T. Li, Y. Wu, and H. Ouyang, “Numerical investigation of tip clearance effects on rotating instability of a low-speed compressor,” *Aerosp Sci Technol*, vol. 111, no. 106540, Apr. 2021, doi: 10.1016/j.ast.2021.106540.

[21] Ansys, “Ansys TurboGrid User’s Guide,” 2024.

[22] Ansys, “Ansys Meshing User’s Guide,” 2021.

[23] W. Yan *et al.*, “Numerical Simulation of Transonic Compressors with Different Turbulence Models,” *Aerospace*, vol. 10, pp. 784–800, Oct. 2023, doi: 10.3390/aerospace10090784.

[24] F. R. Menter, “Two-equation eddy-viscosity turbulence models for engineering applications,” *AIAA Journal*, vol. 32, no. 8, pp. 1598–1605, 1994, doi: 10.2514/3.12149.